

Zircon U–Pb geochronological, trace element, and Hf isotopic constraints on the genesis of the Fe and Cu skarn deposits in the Qiman Tagh area, Qinghai Province, Eastern Kunlun Orogen, China



Lei Yao^{a,b,c}, Zhicheng Lü^{a,c,*}, Caisheng Zhao^d, Zhenshan Pang^{a,c}, Xiaofei Yu^{a,c}, Tao Yang^e, Yongsheng Li^{a,c}, Peng Liu^b, Mingchao Zhang^{a,b,*}

^a Development and Research Center, China Geological Survey, Beijing 100037, People's Republic of China

^b Faculty of Geosciences and Resources, China University of Geosciences, Beijing 100083, People's Republic of China

^c Mineral Exploration Technical Guidance Center, Ministry of Land and Resources of the People's Republic of China (MLR), Beijing 100120, People's Republic of China

^d Technology and International Cooperation Division, Ministry of Land and Resources of the People's Republic of China (MLR), Beijing 100034, People's Republic of China

^e Xi'an Center of Geological Survey, China Geological Survey, Xi'an 710054, People's Republic of China

ARTICLE INFO

Keywords:

Fe skarn deposit
Cu skarn deposit
Zircon Hf isotope
Magma source
Qiman Tagh
Eastern Kunlun Orogen

ABSTRACT

Fe and Cu skarn deposits are very important skarn types worldwide, but it is currently unclear whether the nature of intrusions related to Fe and Cu skarn deposits exerts a key influence on variations in metal associations between Fe and Cu skarn deposits. The Qiman Tagh area of Qinghai Province (QTQP), located in the Eastern Kunlun Orogen (EKO), provides a good opportunity to address this issue. Here, integrating new zircon U–Pb ages, trace elements and Hf isotopes from this study with published data, we constrain the sources of magma associated with Fe and Cu skarn deposits within the QTQP and discuss their role in controlling differences between Fe and Cu skarn deposits.

Combined with published data, two discrete suites of the intrusions associated Fe and Cu skarn deposits have been recognized in the QTQP: (1) 245.1 ± 1.5 Ma granodiorite (related to a 245.5 ± 1.6 Ma Cu skarn deposit) has zircon $\epsilon\text{Hf(t)}$ values of -11.9 to -2.1 ; (2) 235 – 224 Ma monzonites, quartz monzonites, granodiorite porphyries, monzogranites, and granites associated with 234 – 225 Ma Fe skarn deposits are characterized by relatively high zircon $\epsilon\text{Hf(t)}$ values (-5.1 to $+5.9$). The Sr–Nd–Hf isotopic data suggest that the intrusions of Suite 1 and 2 were dominantly derived by partial melting of a Mesoproterozoic juvenile mafic lower crust. Suite 2 intrusions associated with Fe skarn deposits have more mantle components in their magma sources than rocks of Suite 1 that are related to a Cu skarn deposit. Furthermore, zircon $\epsilon\text{Hf(t)}$ values of intrusions associated with Fe and Cu skarn deposits in the QTQP show a negative correlation between mantle components in the magma sources and the contents of Cu and Zn in these deposits. Zircon trace elements indicate that the intrusions associated with Fe skarn deposits are relatively less oxidized than the rock associated with Cu skarn deposit in the QTQP, reflecting a positive correlation between crustal components in the magma sources and oxygen fugacity of the magmas. This indicates that different proportions of mantle and crustal materials in the magma sources may affect oxygen fugacity and Fe contents of the magmas, which possibly leads to the variations in metal associations between Fe and Cu skarn deposits in the QTQP. Zircon U–Pb ages, trace elements and Hf isotopic compositions, combined with geological, geochronological, and geochemical evidence, indicates that having different proportions of mantle components in the magma sources of intrusions associated with Fe and Cu skarn deposits is one of the most critical factors controlling differences in metal association between Fe and Cu skarn deposits.

1. Introduction

The Fe and Cu skarn deposits are the most important skarn types worldwide (Meinert et al., 2005), and are economically important in

China (Zhao et al., 2012). Fe skarn deposits consist dominantly of magnetite, and some deposits which contain significant amounts of Cu are transitional to more typical Cu skarns (Meinert et al., 2005). The common features of Fe and Cu skarn deposits have been extensively

* Corresponding authors at: Development and Research Center, China Geological Survey, No. 45 Fuwai Street, Xicheng District, Beijing 100037, People's Republic of China.
E-mail addresses: zhichengl@163.com (Z. Lü), cgszhangmc@163.com (M. Zhang).

summarized (e.g., Einaudi et al., 1981; Einaudi and Burt, 1982; Meinert et al., 2005), but critical factors controlling differences in metal association between Fe and Cu skarn deposits have been poorly constrained (e.g., Meinert, 1992, 1995; Meinert et al., 2005; Xie et al., 2015, 2016). Stable isotope and fluid inclusion studies indicate that the metal contents of almost all large skarn deposits are directly derived from an igneous source (e.g., Shimazaki and Yamamoto, 1983; Meinert, 1995; Bowman, 1998; Meinert et al., 2003, 2005; Zhou et al., 2007; Xie et al., 2016), and thus the relationship between skarn types and various igneous rocks can be used as a proxy to evaluate the petrogenesis of skarn deposits (e.g., Zharikov, 1970; Kwak and White, 1982; Nakano et al., 1990; Meinert, 1993, 1995; Ray et al., 1995; Kuçcu et al., 2002, 2004; Pons et al., 2010; Yao et al., 2015a,b; Xie et al., 2011, 2016). Meinert (1995) summarized major and trace element geochemical data for plutons related to skarn deposits worldwide, and proposed that intrusions associated with Fe skarn deposits have a greater component of mantle melts compared to Cu skarn deposits. In addition, Pons et al. (2010) reviewed the geology, petrography, and geochemistry of igneous rocks related to Fe, Au, and Cu skarns in the Andes Cordillera of Argentina, and also suggested that the magma sources of intrusions related to Fe skarn deposits were more primitive than intrusions associated with Cu skarn deposits. However, recent Sr–Nd–Hf isotopic data showed that intrusions associated with Fe skarn deposits involved more crustal materials in the magma sources than intrusions related to Cu–Fe skarn deposits in the Edong ore district, eastern China (Xie et al., 2011, 2015). Consequently, it is vital to clarify whether different proportions of mantle and crustal materials in magma sources play an essential role in controlling differences between Fe and Cu skarn deposits.

The Eastern Kunlun Orogen (EKO) is one of the most important metallogenic provinces in China, and most ore deposits in the region are associated with Early Mesozoic magmatism (Mao et al., 2012; Xia et al., 2015a; Yu et al., 2017). The Qiman Tahg area of Qinghai Province (QTQP), located in the western margin of the EKO, is the most important Fe and Cu skarn belt in western China (Zhao et al., 2013). There are some important Fe, Fe–Zn, and Fe–Cu–Zn deposits in the QTQP, which are mined predominantly for magnetite (Yu et al., 2015a; Zuo et al., 2015), and are referred as Fe skarn deposits in this study. The Cu skarn deposit is mined for ores of Cu and contains some Zn and Mo. Most polymetallic skarn deposits in the QTQP are related to Triassic intrusions (e.g., Feng et al., 2012; Mao et al., 2012; Zhao et al., 2013; Yao et al., 2015b). However, the relationship between Fe and Cu skarn deposits and magma sources of mineralization-related intrusions in the study area has rarely been discussed.

Zircon Hf isotopes have been widely used in tracing magma sources and petrogenetic processes for granitoids (e.g., Griffin et al., 2002; Wu et al., 2007; Yang et al., 2007; Qiu et al., 2016) and can provide more stable and robust constraints on the relative contributions of mantle and crustal materials in magma sources than does the traditional approach based on petrology, geochemistry, and Sr–Nd isotopes of whole rocks (Belousova et al., 2006; Goodge and Vervoort, 2006; Murgulov et al., 2008). Additionally, zircon trace elements can provide important information on the temperature and oxidation state of magma sources (e.g., Pettke et al., 2005; Ferry and Watson, 2007; Trail et al., 2012). However, surprisingly few zircon Hf isotopic and trace element studies have been attempted to clarify the relationship between skarn types and magma sources (Meinert et al., 2005; Xie et al., 2015). In this study, we present new zircon U–Pb, trace element, and Hf isotopic data of intrusions associated with the Fe and Cu skarn deposits in the QTQP. Combined with previous published data, this paper provides important constraints on magma sources of intrusions associated with Fe and Cu skarn deposits in the QTQP and their role in controlling differences between Fe and Cu skarn deposits.

2. Geological background

The EKO is bound to the north by the Qaidam Basin (QDM; Fig. 1a),

to the south by the Baryan Har–Songpanganzi Terrane (BH–SG) and South Kunlun–Anyemagen Fault (S. KLF–AMF), to the west by the Altyn Tagh Fault (ATF; Fig. 1a), and to the east by the western Qinling Orogen. The Middle Kunlun Fault (M. KLF) separates the EKO into the North Kunlun Terrane (NKT) and the South Kunlun Terrane (SKT) (Fig. 1a; Xu et al., 2007). The NKT is characterized by Early Paleozoic and Early Mesozoic granitic intrusions (Xu et al., 2007). The terrane consists of metamorphosed Paleo- and Mesoproterozoic amphibolite–granulite facies rocks of the Jinshukou Group, Sinian to Silurian clastic and carbonate rocks, Late Devonian clastic rocks and terrestrial volcanic rocks, and Carboniferous to Permian clastic rocks. The SKT contains Sinian to Cambrian gneiss, schist, migmatites, and amphibolite of the Kuhai Group, Late Devonian clastic and volcanic rocks, and Carboniferous to Triassic marine sedimentary formations. In addition, Triassic granitic intrusions were also developed in the terrane (Jiang et al., 1992; Xu et al., 2007).

The QTQP is located within the NKT (Fig. 1b), and contains Paleoproterozoic to Mesoproterozoic gneiss of the Jinshukou Group, Mesoproterozoic Xiaomiao Group schist and quartzite, Mesoproterozoic Langyashan Group carbonate rocks, Ordovician to Silurian clastic, carbonate and volcanic rocks of the Tanjianshan Group, Devonian clastic and volcanic rocks of the Maoniushan Formation, Carboniferous to Permian clastic and carbonate rocks, and Late Triassic volcanic rocks of the Elashan Formation. The Elashan Formation is widespread and consists of rhyolite, rhyolitic tuff, and dacite. The volcanic rocks of the Formation have been dated at 222 to 208 Ma using the whole rock Rb–Sr method (Liu, 2001). Late Paleozoic and Early Mesozoic igneous rocks are volumetrically dominant, and mainly consist of Devonian to Triassic granitic intrusions.

Triassic granitoids are widely developed throughout the QTQP (Fig. 1b). Early Triassic granitic rocks locally exposed; they consist of monzogranite and granodiorite. Middle Triassic granitoids are characterized by containing numerous mafic micro-granular enclaves (MMEs) (Feng et al., 2012). These rocks occur as batholiths, and are dominantly diorite, quartz diorite, and granodiorite. Late Triassic granitic intrusions are most widespread and mainly consist of granodiorite, monzogranite, monzogranite porphyry, granite, and granite porphyry. Compared to the Middle Triassic granitic intrusions, the Late Triassic granitic rocks occur as batholiths, stocks and dikes, and lack MMEs (Guo et al., 1998; Feng et al., 2012).

The geological features of Fe and Cu skarn deposits in the QTQP have been extensively studied, and major reviews include Feng et al. (2012), Mao et al. (2012), and Zhao et al. (2013). These deposits were discovered along the contact between Paleoproterozoic to Carboniferous carbonate rocks and Triassic granitic rocks, mostly at the intersections of faults and folds that trend NWW, NW, and EW (Zhao et al., 2013). The Fe skarn deposits are mined for magnetite, and some deposits contain significant amounts of Cu and Zn, including Kendekeke Fe, Yemaquan Fe–Cu–Zn, Galinge Fe–Zn and Tawenchahanxi Fe–Cu–Zn deposits (Zhao et al., 2013), and several small Fe–Cu–Zn deposits in the Hutouya ore field (Zhang et al., 2013). The Kaerqueka deposit is the only large porphyry-skarn Cu deposit so far discovered in the QTQP and the skarn ores were associated with granodiorite in the deposit (Feng et al., 2012). In addition, some porphyry Cu–Mo–Ag and porphyry-skarn Mo deposits occur around Triassic granitoids (e.g., Chen et al., 2013; Zhao et al., 2013; Xu et al., 2014; Yao et al., 2015b; Fig. 1b).

3. Comparison of the composition of the intrusions associated with Fe and Cu skarn deposits in the QTQP with “world-wide” Fe and Cu skarn granitoids

The igneous rocks associated with Fe and Cu skarn deposits in the QTQP share several major and trace element geochemical features with intrusive rocks associated with Fe and Cu skarn deposits worldwide (Fig. 2; Meinert, 1995). Most of these rocks are high-K calc-alkaline,

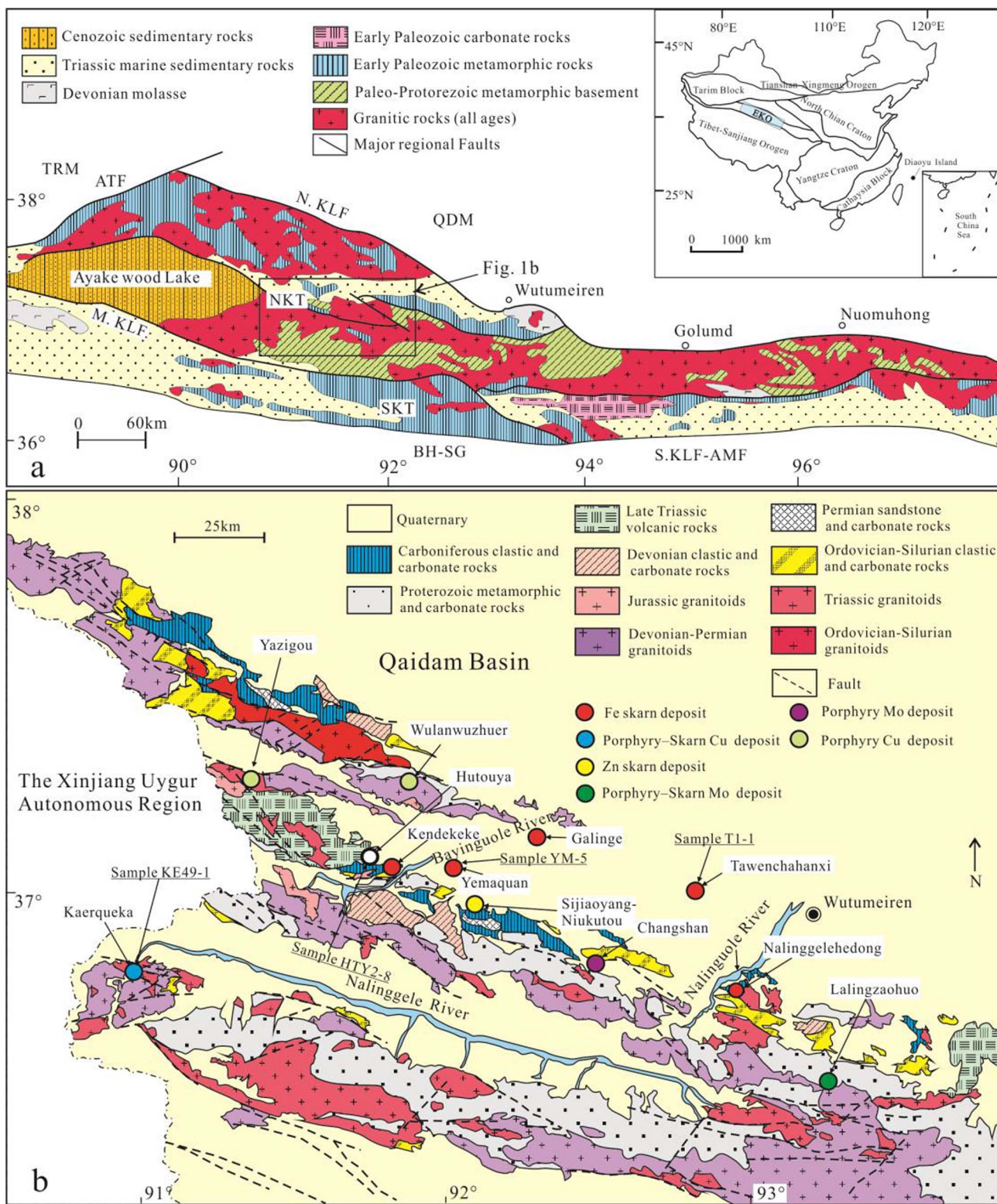


Fig. 1. (a) Sketch geological map of the EKO (modified from Xu et al., 2007; Ding et al., 2014); (b) Geological map showing the main type of mineral deposits in the QTQP (modified from Yao et al., 2015b).

except for the Galinge quartz monzonites which plot in the field of tholeiitic (Fig. 2a). They are subalkaline and range from tonalite and monzonite to granodiorite and granite compositions in the SiO_2 vs. ($\text{K}_2\text{O} + \text{Na}_2\text{O}$) diagram (Fig. 2b). In the AFM diagram (Fig. 2c), the igneous rocks are subalkaline with a calc-alkaline affinity, similar to most plutons related to Fe and Cu skarn deposits (Meinert, 1995).

According to the A/CNK vs. A/NK diagram (Fig. 2d), the Galinge quartz monzonites and Yemaquan monzonites are situated in the metaluminous field, whereas other intrusions are metaluminous to weakly peraluminous. Furthermore, almost all the intrusions contain hornblende, biotite, and accessory magnetite and titanite, and have relatively low P_2O_5 contents, and $\text{FeO}^\text{T}/\text{MgO}$ and $(\text{Zr} + \text{Ce} + \text{Nb} + \text{Y})$ values (Xi et al.,

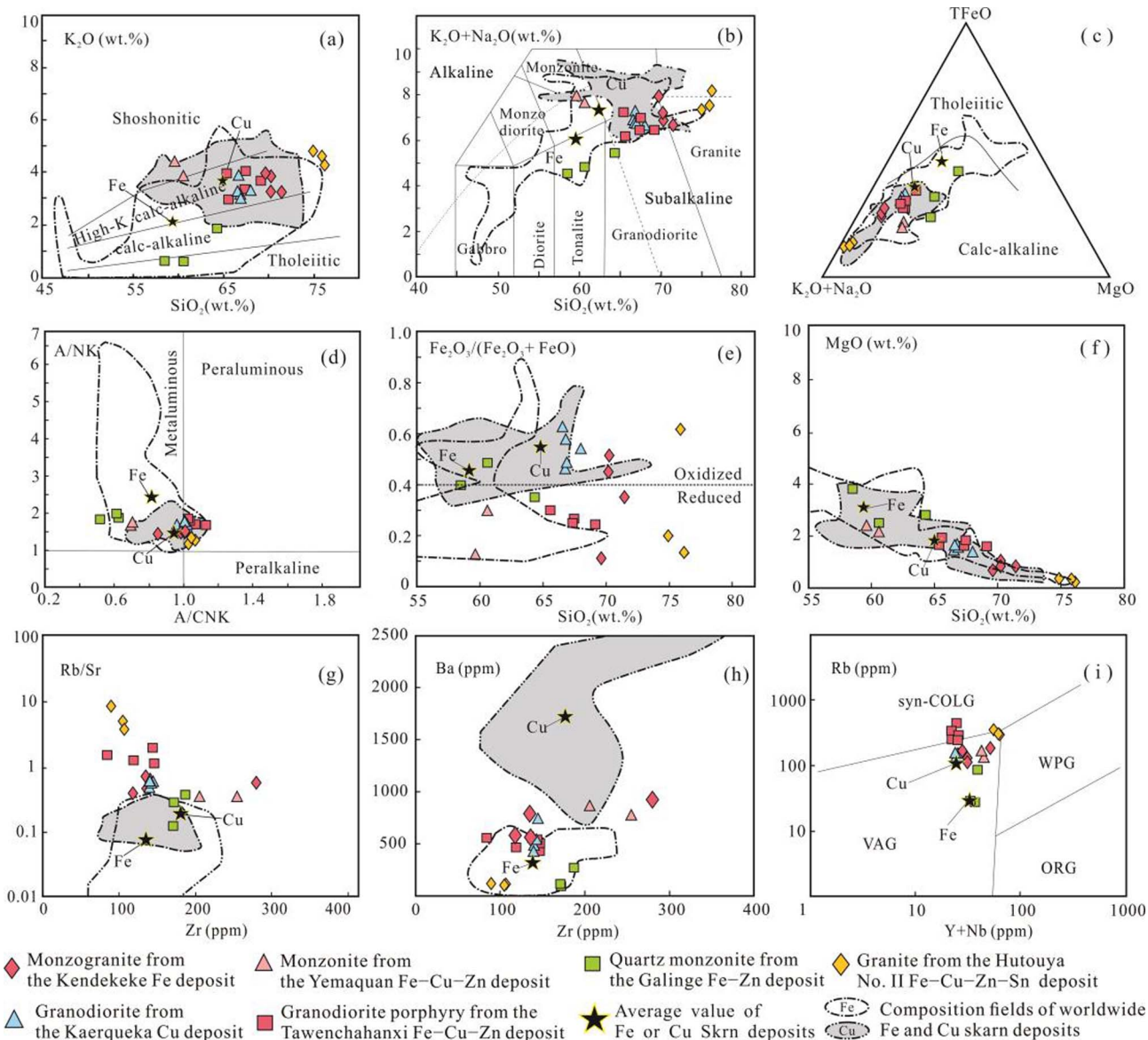


Fig. 2. Geochemical characteristics of the intrusions associated with Fe and Cu skarn deposits in the QTQP. (a) SiO_2 vs. K_2O (Le Maitre, 1989); (b) SiO_2 vs. $(\text{K}_2\text{O} + \text{Na}_2\text{O})$; (c) AFM diagram with tholeiitic and calc-alkaline fields from Irvine and Baragar (1971); (d) A/NK vs. A/CNK ; (e) SiO_2 vs. $\text{Fe}_2\text{O}_3/(\text{Fe}_2\text{O}_3 + \text{FeO})$; (f) SiO_2 vs. MgO ; (g) Rb/Sr vs. Zr ; (h) Ba vs. Zr ; (i) Rb vs. $(\text{Y} + \text{Nb})$ diagram (Pearce et al., 1984) with fields of within-plate granites (WPG), volcanic arc granites (VAG), syn-collision granites (Syn-COLG), and ocean ridge granites (ORG). Average values of major and trace element contents and the compositional fields of plutons associated with Fe and skarn deposits worldwide (Meinert, 1995; Pons et al., 2010) are shown for comparison. Major and trace element data of the Yemaquan monzonite, Kaerqueka granodiorite, Hutouya granite, Tawenchahanxi granodiorite porphyry, Kendekeke monzogranite, and Galinge quartz monzonite are from Xi et al. (2010), Gao et al. (2012), Yang (2015) and Yao (2015).

2010; Gao et al., 2012; Yang, 2015; Yao, 2015). These features are similar to those of I-type granite (Chappell and White, 2001). The intrusions associated with Fe skarn deposits have relatively lower $\text{Fe}_2\text{O}_3/(\text{Fe}_2\text{O}_3 + \text{FeO})$ ratios than those of rocks related to Cu skarn deposit, which exhibit $\text{Fe}_2\text{O}_3/(\text{Fe}_2\text{O}_3 + \text{FeO})$ ratios in the 0.5–0.6 range (Fig. 2e). This suggests that the magma of the latter is more oxidized than that of the former, which is similar to plutons associated with Fe and Cu skarns worldwide (Meinert, 1995). In the MgO vs. SiO_2 diagram (Fig. 2f), all the intrusions have MgO contents similar to those of intrusive rocks related to Fe and Cu skarns (Meinert, 1995). The Galinge quartz monzonites and Yemaquan monzonites have relatively higher MgO and lower SiO_2 contents than other rocks (Fig. 2f), indicating a relatively more primitive magma source.

The intrusions associated with Fe and Cu skarn deposits in the QTQP have low Sr/Y and $(\text{La/Yb})_N$ ratios and high Y and Yb contents (Xi et al., 2010; Gao et al., 2012; Yang, 2015; Yao, 2015), which show affinity to arc magmas. In the Rb/Sr vs. Zr diagram (Fig. 2g), most rocks have

relatively higher Rb/Sr ratios than those of intrusions associated with Fe and Cu skarn deposits worldwide, indicating that these rocks have undergone differentiation processes. In the Ba vs. Zr diagram (Fig. 2h), except for the Yemaquan monzonite and Kendekeke monzogranite, almost all the rocks have relatively low Ba contents and plot in the field of intrusions associated with Fe skarn, which is probably the result of significant degrees of plagioclase and K-feldspar fractionation. In the Rb vs. $(\text{Y} + \text{Nb})$ diagram (Fig. 2i), most rocks plot in the field of volcanic arc granitoids, except for the Tawenchahanxi granodiorite porphyry that plots in the field of syn-collision granites.

4. Petrography and sampling

Monzonite sample (YM-5) was collected from drill hole ZK11304 in the Yemaquan Fe-Cu-Zn deposit. The monzonite is medium-grained and massive, and predominantly comprises quartz (5–10%), plagioclase (35–40%), K-feldspar (40–45%), and biotite (~5%). The accessory

minerals are zircon, magnetite, and titanite.

Granodiorite sample (KE49-1) was collected from the Kaerqueka Cu deposit, and is characterized by a medium-grained texture, consisting of quartz (20–25%), plagioclase (45–50%), K-feldspar (15–20%), amphibole (5–10%), biotite (~5%), and accessory zircon, magnetite, and titanite.

Granite sample (HTY2-8) was collected from the No. II Fe-Cu-Zn-Sn deposit in the Hutouya ore field (Hutouya No. II Fe-Cu-Zn-Sn deposit), and is fine to medium grained, and dominated by quartz (25–30%), K-feldspar (45–50%), plagioclase (15–20%), and biotite (5–10%), and accessory zircon, titanite, and apatite.

Granodiorite porphyry sample (T1-1) was collected from drillhole ZK25408 in the Tawenchahanxi Fe-Cu-Zn deposit and is characterized by medium- to coarse- grained and porphyritic texture, consisting of quartz (~25%), plagioclase (~50%), K-feldspar (~15%), and biotite (~7%) with minor amphibole (~3%). Accessory minerals include zircon, titanite, apatite, and magnetite.

5. Analytical methods

5.1. Zircon U-Pb dating and trace element analyses

Zircons were separated by conventional heavy liquid and magnetic techniques. Single zircons were handpicked using a binocular microscope, mounted in epoxy resin, and then polished to expose grain centers. Zircons for U-Pb isotopic analyses were selected under transmitted and reflected light, and then imaged by cathodoluminescence (CL) using a JEOL JSM-6510 microprobe at Beijing GeoAnalysis Co., Ltd.

Zircon U-Pb dating was conducted by laser ablation-inductively coupled plasma-mass spectrometry (LA-ICP-MS), using a New Wave UP213 laser attached to a Neptune multi-collector ICP-MS at the Institute of Mineral Resources of the Chinese Academy of Geological Sciences (CAGS), Beijing, China. Details about instrumental protocols and data acquisition methods are given in Hou and Yuan (2010). Helium was used as a carrier gas to enhance the transport efficiency during ablation. U, Th, and Pb concentrations are calculated by using the standard silicate glass NIST SRM 610. Zircon GJ1 standard was applied as an external calibration standard, and was analyzed twice every 10 analyses during U-Pb dating. U-Th-Pb isotopic ratios used for GJ1 are from Jackson et al. (2004). ISOPLOT/Ex (v. 3.0) (Ludwig, 2003) was used for U-Pb age calculation and concordia diagram construction. The zircon Plesovice is dated as unknown samples and yielded weighted mean $^{206}\text{Pb}/^{238}\text{U}$ age of 337 ± 4 Ma (2σ , $n = 10$), which agrees with the recommended values within 2σ error (337.13 ± 0.37 Ma; Sláma et al., 2008). Zircon trace element analyses were obtained by LA-ICP-MS at the State Key Laboratory of Geological Processes and Mineral Resources of the China University of Geosciences (CUG), Wuhan. The NIST 612 was used as a reference material for calibration. More detailed operating conditions for the laser ablation system and the ICP-MS instrument and data reduction are described by Liu et al. (2008, 2010). ICPMSDataCal were used to perform the off-line selection and integration of background and analytical signals, and the time-drift correction and quantitative calibration of trace element analyses (Liu et al., 2008, 2010).

5.2. Zircon Hf isotopic analysis

Zircon Hf isotopic analyses were performed on the same spots where U-Pb age determinations were undertaken. Zircon Hf isotopes were determined with a New Wave UP213 laser-ablation microprobe attached to a Neptune multi-collector ICP-MS at the State Key Laboratory of Geological Processes and Mineral Resources, CUG, Wuhan and the Institute of Mineral Resources of the CAGS, Beijing. Instrumental conditions and data acquisition were described by Wu et al. (2006) and Hou et al. (2007). Zircons were ablated with a beam diameter of

~55 μm, using helium as the carrier gas combined with argon to transport the ablated sample into the ICP-MS torch. The isobaric interferences of ^{176}Lu and ^{176}Yb on ^{176}Hf was corrected by determining the $^{176}\text{Lu}/^{175}\text{Lu} = 0.02658$ and $^{176}\text{Yb}/^{173}\text{Yb} = 0.796218$ ratios (Chu et al., 2002). Yb isotope ratios and Hf isotope ratios were normalized to $^{172}\text{Yb}/^{173}\text{Yb} = 1.35274$ (Chu et al., 2002) and $^{179}\text{Hf}/^{177}\text{Hf} = 0.7325$ by using an exponential law to correct instrumental mass bias. Zircon Penglai was used as external standard for Hf isotopic analyses, and gave a weighted mean $^{176}\text{Hf}/^{177}\text{Hf}$ ratio of 0.282910 ± 0.000014 (2σ , $n = 19$), indistinguishable from the recommended $^{176}\text{Hf}/^{177}\text{Hf}$ value of 0.282906 ± 0.0000010 (2σ) (Li et al., 2010). Zircon GJ1 was also used as the reference standard, with a weighted mean $^{176}\text{Hf}/^{177}\text{Hf}$ ratio of 0.281996 ± 0.000013 (2σ , $n = 10$) which agrees with the weighted mean $^{176}\text{Hf}/^{177}\text{Hf}$ ratio of 0.282000 ± 0.000005 (2σ) using a solution analysis method (Morel et al., 2008).

6. Results

6.1. Zircon U-Pb ages

Zircons from the monzonite (sample YM-5) in the Yemaquan Fe-Cu-Zn deposit are 100–200 μm long, 90–100 μm wide, and are subhedral to euhedral, colorless, prismatic, with oscillatory zoning in CL images (Fig. 3a), indicative of a magmatic origin (Hoskin and Black, 2000). Twenty zircons were analyzed and the results show high Th (124–1156 ppm) and U (243–1057 ppm) concentrations, and moderate Th/U ratios (0.4–2.5) (Table 1). All 20 zircon analyses yield a concordant weighted mean $^{206}\text{Pb}/^{238}\text{U}$ age of 223.5 ± 1.7 Ma (MSWD = 0.7, $n = 20$; Fig. 4a), which provides the crystallization age of the monzonite in the Yemaquan deposit.

Zircons separated from the granodiorite (sample KE49-1) in the Kaerqueka Cu deposit are euhedral, 100–190 μm long, and 40–110 μm wide. The CL images show that the zircons are oscillatory zoned (Fig. 3b). Fifteen zircons were analyzed and the results show moderate Th (304–726 ppm) and U (553–1338 ppm) concentrations, and Th/U ratios (0.4–0.8) (Table 1), indicative of a magmatic origin (Hoskin and Black, 2000). All 15 zircons from sample KE49-1 yield a weighted mean $^{206}\text{Pb}/^{238}\text{U}$ age of 245.1 ± 1.5 Ma (MSWD = 0.2, $n = 15$; Fig. 4b), which is interpreted as the crystallization age.

Zircons from the granite (sample HTY2-8) in the Hutouya No. II Fe-Cu-Zn-Sn deposit are mostly euhedral and prismatic, and are 100–180 μm long and 50–100 μm wide. They are oscillatory zoned in CL images (Fig. 3c). Seventeen analyses were obtained on 17 zircon grains. The results show that all the zircons have relatively high contents of Th (192–3792 ppm) and U (396–11509 ppm), and moderate Th/U ratios (0.3–0.7) (Table 1). These features are indicative of a magmatic origin (Hoskin and Black, 2000). All 17 analyses form a coherent group and yield a weighted mean $^{206}\text{Pb}/^{238}\text{U}$ age of 231.7 ± 2.1 Ma (MSWD = 2.0, $n = 17$) (Fig. 4c), which represents the crystallization age of the granite.

Zircons separated from the granodiorite porphyry (sample T1-1) in the Tawenchahanxi Fe-Cu-Zn deposit show oscillatory zoning in CL images (Fig. 3d), and are euhedral and prismatic, with lengths of 100–280 μm, widths of 90–110 μm. The data of 28 analyses undertaken on 28 zircon grains show high contents of Th (194–663 ppm) and U (424–1089 ppm), with Th/U ratios of 0.4–0.7 (Table 1), indicating a magmatic origin (Hoskin and Black, 2000). Twenty-eight analyses form a coherent group with a concordant weighted mean $^{206}\text{Pb}/^{238}\text{U}$ age of 233.5 ± 0.9 Ma (MSWD = 0.3, $n = 28$) (Fig. 4d), which is interpreted to be the crystallization age of the granodiorite porphyry.

6.2. Zircon trace elements and $\text{Ce}^{4+}/\text{Ce}^{3+}$ ratios

The results of zircon trace elements (including rare earth elements, Ti, Hf, Th, U, Nb, Ta, and Y) are presented in Table 2. All the zircons are characterized by enrichment of HREE relatively to LREE, with negative

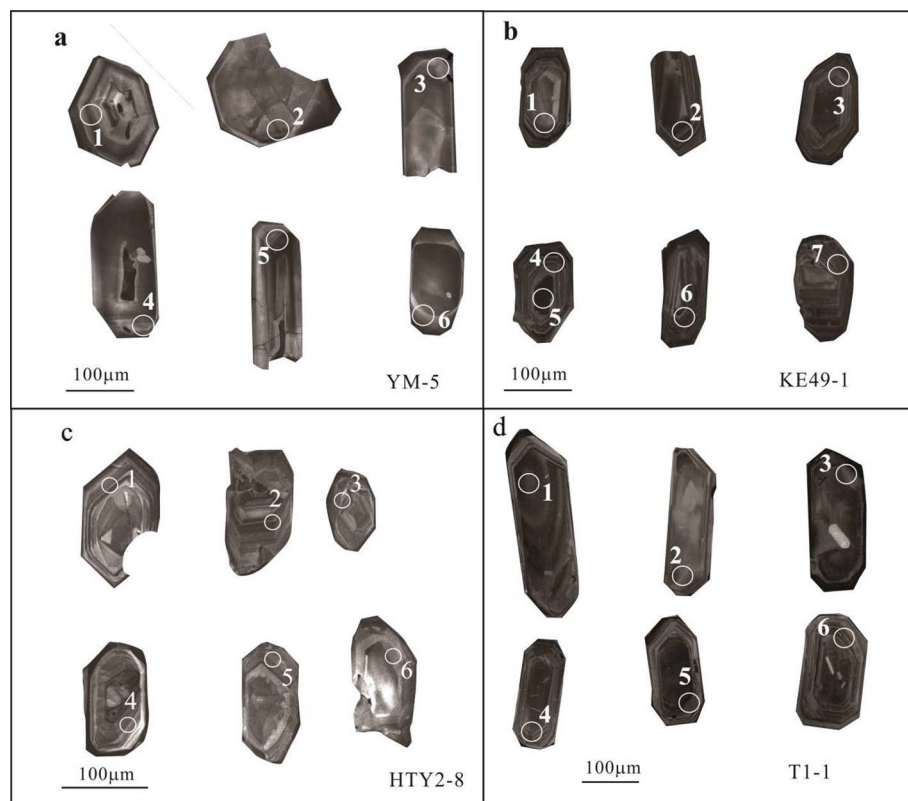


Fig. 3. Representative CL images of zircon grains from (a) Yemaquan monzonite, (b) Kaerqueka granodiorite, (c) Hutouya granite, and (d) Tawenchahanxi granodiorite porphyry.

Eu and positive Ce anomalies (Fig. 5). The chondrite-normalized Ce anomaly (Ce_N/Ce_N^* , where $Ce_N^* = (La_N \times Pr_N)^{1/2}$) of the Kaerqueka granodiorite, Tawenchahanxi granodiorite porphyry, Hutouya granite, and Yemaquan monzonite ranges from 21.8 to 93.4, 23.1 to 57.5 (except one zircon with a high Ce_N/Ce_N^* value of 125), 12.9 to 77.1, and 7.97 to 77.4, respectively (Table 2). Ce^{4+}/Ce^{3+} ratio can be used as an indicator for evaluating oxygen fugacity (e.g., Pettke et al., 2005), because Ce^{4+} can easily substitute Zr^{4+} of zircon under oxidizing condition. The average Ce^{4+}/Ce^{3+} ratios of zircons from the Kaerqueka granodiorite, Tawenchahanxi granodiorite porphyry, Hutouya granite, and Yemaquan monzonite are 240, 135, 41.7, and 37.0, respectively (Table 2), exhibiting a decreasing trend. In addition, Ce/Nd ratio can be also utilized to reflect the oxidation state of magma (Meng et al., 2016), especially when La and Pr are not well determined (Chelle-Michou et al., 2014; Zhang et al., 2017). In Fig. 6, obviously positive correlation between Ce/Nd , and Ce^{4+}/Ce^{3+} and Ce_N/Ce_N^* suggest that both Ce^{4+}/Ce^{3+} and Ce/Nd ratios are suitable for evaluating the oxidation state of the magmas in this study. The Ce^{4+}/Ce^{3+} and Ce/Nd ratios of zircons indicate that oxygen fugacity decreases from the Kaerqueka granodiorite, to Tawenchahanxi granodiorite porphyry, to Hutouya granite, and then to Yemaquan monzonite (Fig. 6).

6.3. Zircon Hf isotopic data

In situ Hf isotopic data for zircons from the Yemaquan monzonite, Kaerqueka granodiorite, Hutouya granite, and Tawenchahanxi granodiorite porphyry are listed in Table 3. The Yemaquan monzonite yielded homogeneous Hf isotopic compositions, with $(^{176}\text{Hf}/^{177}\text{Hf})_i$ ratios ranging from 0.282580 to 0.282678 and $\epsilon\text{Hf}(t)$ values of -1.9 to $+1.6$ ($n = 20$). Zircons from the granodiorite (sample KE49-1) at Kaerqueka yielded $(^{176}\text{Hf}/^{177}\text{Hf})_i$ ratios and $\epsilon\text{Hf}(t)$ values varying from 0.282285 to 0.282560 and -11.9 to -2.1 ($n = 15$), respectively. Zircons from the Hutouya granite (sample HTY2-8) have $(^{176}\text{Hf}/^{177}\text{Hf})_i$ ratios varying from 0.282541 to 0.282658 and give $\epsilon\text{Hf}(t)$ values of -3.1 – $+1.1$ ($n = 15$). The Tawenchahanxi granodiorite porphyry

(sample T1-1) have narrow range of $(^{176}\text{Hf}/^{177}\text{Hf})_i$ ratios (0.282513–0.282589) and yielded $\epsilon\text{Hf}(t)$ values ranging from -4.1 to -1.3 ($n = 17$).

7. Discussion

7.1. Timing of intrusions associated with Fe and Cu skarn deposits

Field relationships and radiometric data suggest that Fe and Cu skarn deposits in the QTQP are associated with Triassic intrusions (Mao et al., 2012; Zhao et al., 2013). However, due to multiple intrusions and low density of sampling, the geochronological framework of the Fe and Cu skarn mineralization, and associated intrusions in the QTQP, this association is still not well established.

The age obtained in the present study for the Kaerqueka granodiorite (245.1 ± 1.5 Ma) is the same (within error) as the molybdenite Re–Os age (245.5 ± 1.6 Ma) of Gao (2013), obtained from the Cu skarn mineralization at Kaerqueka. This new age is also consistent (within error) with the zircon LA–ICP–MS U–Pb age (242.6 ± 3.4 Ma; Chen et al., 2013) of the granodiorite associated with the Lalingzaohuo Mo skarn–porphyry deposit (with a molybdenite Re–Os age of 240.8 ± 4.0 Ma; Wang et al., 2013) (Fig. 7). However, this age is older than previously reported zircon LA–ICP–MS and SHIRMP U–Pb ages (236.9 ± 1.7 Ma to 234.1 ± 0.6 Ma; Wang et al., 2009; Gao et al., 2015) for the granodiorites at Kaerqueka. Recent studies indicate that the Early–Middle Triassic (~237 Ma) and Late Triassic intrusions (ca. 237–204 Ma) were associated with different magmatism and tectonic settings in the QTQP (Mo et al., 2007; Yao, 2015; Yu et al., 2017). This implies that the granodiorites in this paper and previous studies may represent two distinct episodes of magmatism (Fig. 7). Field investigations reveal that skarn orebodies were developed along the contacts between the granodiorite and the marble, and the endoskarns are well developed within the granodiorite. Thus, considering the temporal, spatial, and genetic relationships between granodiorite and the Cu skarn mineralization at Kaerqueka (Wang et al., 2009; Feng

Table 1

LA-ICP-MS U-Pb data for zircons from the Yemaquan monzonite, Kaerqueka granodiorite, Hutouya granite, and Tawenchahanxi granodiorite porphyry in the QTQP.

Spot	Th (ppm)	U (ppm)	Th/U	$^{207}\text{Pb}/^{206}\text{Pb}$	1 σ	$^{207}\text{Pb}/^{235}\text{U}$	1 σ	$^{206}\text{Pb}/^{238}\text{U}$	1 σ	$^{207}\text{Pb}/^{206}\text{Pb}$ age	1 σ	$^{207}\text{Pb}/^{235}\text{U}$ age	1 σ	$^{206}\text{Pb}/^{238}\text{U}$ age	1 σ
										(Ma)		(Ma)		(Ma)	
YM-5 (monzonite)															
1	232	406	0.6	0.0549	0.0038	0.2755	0.0188	0.0364	0.0010	406	156	247	15	230	6
2	685	865	0.8	0.0510	0.0018	0.2456	0.0084	0.0349	0.0005	239	75	223	7	221	3
3	298	448	0.7	0.0524	0.0030	0.2548	0.0146	0.0350	0.0007	302	131	230	12	222	5
4	280	478	0.6	0.0499	0.0022	0.2405	0.0107	0.0351	0.0005	191	108	219	9	222	3
5	124	243	0.5	0.0542	0.0048	0.2765	0.0255	0.0367	0.0010	389	200	248	20	232	6
6	400	564	0.7	0.0476	0.0019	0.2303	0.0100	0.0352	0.0008	80	93	210	8	223	5
7	297	479	0.6	0.0500	0.0022	0.2410	0.0110	0.0351	0.0005	195	104	219	9	222	3
8	469	609	0.8	0.0561	0.0069	0.2809	0.0295	0.0367	0.0014	457	278	251	23	232	9
9	337	875	0.4	0.0526	0.0017	0.2543	0.0093	0.0350	0.0005	322	72	230	8	222	3
10	341	491	0.7	0.0507	0.0022	0.2421	0.0108	0.0350	0.0006	233	98	220	9	222	3
11	712	881	0.8	0.0496	0.0016	0.2424	0.0093	0.0357	0.0007	176	76	220	8	226	4
12	445	573	0.8	0.0493	0.0020	0.2342	0.0102	0.0348	0.0007	161	94	214	8	221	4
13	417	571	0.7	0.0466	0.0018	0.2266	0.0095	0.0354	0.0007	28	89	207	8	224	4
14	233	402	0.6	0.0489	0.0025	0.2379	0.0124	0.0360	0.0008	143	120	217	10	228	5
15	645	873	0.7	0.0501	0.0019	0.2408	0.0098	0.0350	0.0005	198	89	219	8	222	3
16	764	938	0.8	0.0534	0.0022	0.2589	0.0109	0.0352	0.0005	346	94	234	9	223	3
17	341	410	0.8	0.0502	0.0023	0.2420	0.0112	0.0351	0.0005	211	103	220	9	222	3
18	950	1057	0.9	0.0521	0.0018	0.2563	0.0099	0.0354	0.0006	300	80	232	8	225	4
19	481	716	0.7	0.0502	0.0024	0.2459	0.0113	0.0355	0.0005	211	105	223	9	225	3
20	1156	458	2.5	0.0532	0.0023	0.2668	0.0109	0.0376	0.0012	345	98	240	9	238	8
KE49-1 (granodiorite)															
1	433	730	0.6	0.0567	0.0015	0.3051	0.0078	0.0390	0.0005	481	36	270	6	247	3
2	304	553	0.6	0.0525	0.0025	0.2804	0.0129	0.0387	0.0005	309	112	251	10	245	3
3	550	1207	0.5	0.0537	0.0013	0.2877	0.0068	0.0389	0.0004	357	33	257	5	246	3
4	726	945	0.8	0.0514	0.0013	0.2757	0.0069	0.0389	0.0005	259	37	247	6	246	3
5	593	847	0.7	0.0528	0.0025	0.282	0.0128	0.0387	0.0005	321	109	252	10	245	3
6	491	938	0.5	0.0554	0.0025	0.2963	0.0128	0.0388	0.0005	427	103	264	10	246	3
7	597	1045	0.6	0.0514	0.0014	0.2755	0.0071	0.0389	0.0005	261	38	247	6	246	3
8	516	806	0.6	0.0508	0.0026	0.2687	0.0131	0.0384	0.0005	230	118	242	10	243	3
9	380	729	0.5	0.0527	0.0016	0.2812	0.0082	0.0387	0.0005	314	44	252	7	245	3
10	442	802	0.6	0.0529	0.0016	0.2803	0.0081	0.0385	0.0005	323	43	251	6	243	3
11	522	1338	0.4	0.0527	0.0024	0.2829	0.0124	0.0389	0.0005	318	106	253	10	246	3
12	575	943	0.6	0.0522	0.0017	0.2786	0.0090	0.0387	0.0005	296	50	250	7	245	3
13	528	949	0.6	0.0533	0.0017	0.2852	0.0087	0.0388	0.0005	340	46	255	7	246	3
14	409	796	0.5	0.0522	0.0017	0.2778	0.0088	0.0386	0.0005	294	49	249	7	244	3
15	549	1177	0.5	0.0506	0.0016	0.2687	0.0082	0.0385	0.0005	224	47	242	7	243	3
HTY2-8 (granite)															
1	275	711	0.4	0.0530	0.0029	0.2607	0.0150	0.0361	0.0009	328	126	235	12	228	6
2	893	1476	0.6	0.0545	0.0026	0.2499	0.0117	0.0356	0.0015	394	109	226	10	225	9
3	382	830	0.5	0.0559	0.0023	0.2747	0.0108	0.0360	0.0005	456	123	246	9	228	3
4	664	1581	0.4	0.0506	0.0017	0.2456	0.0079	0.0353	0.0005	233	76	223	6	223	3
5	628	1225	0.5	0.0526	0.0017	0.2628	0.0089	0.0362	0.0004	322	74	237	7	229	3
6	603	1204	0.5	0.0526	0.0019	0.2613	0.0095	0.0362	0.0005	309	81	236	8	229	3
7	336	938	0.4	0.0533	0.0043	0.2572	0.0204	0.0357	0.0011	339	188	232	16	226	7
8	519	1045	0.5	0.0521	0.0028	0.2661	0.0132	0.0374	0.0007	287	121	240	11	237	4
9	340	946	0.4	0.0515	0.0045	0.2536	0.0219	0.0361	0.0008	261	199	230	18	229	5
10	342	892	0.4	0.0577	0.0038	0.2755	0.0173	0.0351	0.0006	517	144	247	14	223	4
11	323	933	0.4	0.0543	0.0026	0.2651	0.0141	0.0371	0.0016	383	77	239	11	235	10
12	3792	11509	0.3	0.0523	0.0010	0.2703	0.0062	0.0374	0.0005	298	44	243	5	237	3
13	243	441	0.6	0.0562	0.0021	0.2868	0.0112	0.0370	0.0004	461	83	256	9	234	3
14	250	396	0.6	0.0536	0.0027	0.2724	0.0138	0.0370	0.0005	367	113	245	11	234	3
15	254	453	0.6	0.0547	0.0028	0.2751	0.0130	0.0375	0.0008	467	121	247	10	237	5
16	278	413	0.7	0.0546	0.0028	0.2758	0.0130	0.0377	0.0006	394	117	247	10	239	3
17	192	431	0.5	0.0501	0.0028	0.2581	0.0139	0.0376	0.0006	211	130	233	11	238	4
T1-1 (granodiorite porphyry)															
1	627	1089	0.6	0.0520	0.0010	0.2646	0.0047	0.0369	0.0004	287	43	238	4	234	2
2	257	597	0.4	0.0512	0.0010	0.2619	0.0051	0.0371	0.0004	256	44	236	4	235	2
3	434	746	0.6	0.0510	0.0010	0.2600	0.0049	0.0370	0.0004	243	44	235	4	234	2
4	307	652	0.5	0.0507	0.0011	0.2587	0.0057	0.0370	0.0004	228	52	234	5	234	2
5	267	574	0.5	0.0512	0.0011	0.2606	0.0056	0.0370	0.0004	256	50	235	4	234	2
6	486	1008	0.5	0.0516	0.0009	0.2632	0.0049	0.0369	0.0003	333	41	237	4	234	2
7	203	457	0.4	0.0524	0.0015	0.2660	0.0082	0.0368	0.0004	302	65	239	7	233	3
8	242	540	0.5	0.0513	0.0022	0.2632	0.0106	0.0372	0.0005	376	55	249	5	236	3
9	363	828	0.4	0.0509	0.0009	0.2597	0.0050	0.0370	0.0004	235	41	234	4	234	3
10	510	926	0.6	0.0505	0.0010	0.2587	0.0053	0.0371	0.0004	220	43	234	4	235	3
11	297	636	0.5	0.0532	0.0012	0.2765	0.0063	0.0377	0.0005	345	50	248	5	238	3
12	268	683	0.4	0.0510	0.0012	0.2602	0.0062	0.0369	0.0004	239	58	235	5	234	3
13	298	634	0.5	0.0509	0.0011	0.2582	0.0055	0.0368	0.0005	235	48	233	4	233	3
14	194	484	0.4	0.0511	0.0013	0.2610	0.0066	0.0371	0.0004	256	59	235	5	234	3
15	321	775	0.4	0.0500	0.0010	0.2551	0.0055	0.0369	0.0005	195	44	231	4	234	3

Table 1 (continued)

Spot	Th (ppm)	U (ppm)	Th/U	$^{207}\text{Pb}/^{206}\text{Pb}$	1σ	$^{207}\text{Pb}/^{235}\text{U}$	1σ	$^{206}\text{Pb}/^{238}\text{U}$	1σ	$^{207}\text{Pb}/^{206}\text{Pb}$ age (Ma)	1σ	$^{207}\text{Pb}/^{235}\text{U}$ age (Ma)	1σ	$^{206}\text{Pb}/^{238}\text{U}$ age (Ma)	1σ
16	526	989	0.5	0.0522	0.0009	0.2651	0.0049	0.0368	0.0004	295	45	239	4	233	3
17	351	681	0.5	0.0520	0.0019	0.2619	0.0094	0.0365	0.0004	409	39	249	4	232	2
18	370	619	0.6	0.0515	0.0011	0.2602	0.0059	0.0366	0.0004	265	53	235	5	232	2
19	303	636	0.5	0.0501	0.0014	0.2531	0.0070	0.0368	0.0005	198	31	229	6	233	3
20	280	577	0.5	0.0501	0.0012	0.2546	0.0062	0.0369	0.0004	198	54	230	5	234	2
21	663	1065	0.6	0.0515	0.0008	0.2606	0.0049	0.0367	0.0004	261	32	235	4	232	2
22	390	792	0.5	0.0528	0.0009	0.2677	0.0054	0.0367	0.0004	320	44	241	4	232	2
23	391	729	0.5	0.0509	0.0013	0.2582	0.0064	0.0369	0.0004	235	62	233	5	233	3
24	477	719	0.7	0.0515	0.0015	0.2613	0.0078	0.0368	0.0004	265	69	236	6	233	3
25	259	424	0.6	0.0488	0.0021	0.2468	0.0115	0.0367	0.0007	200	102	224	9	232	4
26	386	696	0.6	0.0523	0.0023	0.2629	0.0113	0.0370	0.0008	295	98	237	9	234	5
27	418	690	0.6	0.0510	0.0012	0.2606	0.0072	0.0370	0.0005	243	56	235	6	234	3
28	472	890	0.5	0.0497	0.0010	0.2499	0.0054	0.0364	0.0004	189	17	227	4	231	3

et al., 2009; Gao, 2013), we believe that the most plausible age for the granodiorite is 245.1 ± 1.5 Ma, as obtained in this study.

For the Fe skarn deposits, our new LA-ICP-MS zircon U-Pb data indicate that the age of the Yemaquan monzonite (223.5 ± 1.7 Ma) is older than the LA-ICP-MS zircon U-Pb ages of the quartz monzodiorite (219 ± 1 Ma) and syenogranite (213 ± 1 Ma) at Yemaquan (Gao et al., 2014). This age is identical (within error) to the well-defined plateau $^{40}\text{Ar}-^{39}\text{Ar}$ age (225 ± 2 Ma; Ma et al., 2015) of phlogopite from magnetite ores in the Yemaquan Fe-Cu-Zn deposit (Fig. 7). Geological features show that orebodies of the Yemaquan deposit in drill hole ZK11304 were developed along the contacts between the monzonite and the marble. This indicates that crystallization of the monzonite and initiation of the Fe-Cu-Zn mineralization at Yemaquan are temporally and genetically related. The orebodies of the Hutouya No. II Fe-Cu-Zn-Sn deposit have granite footwall and marble hangingwall. Moreover, intense contact metasomatism was developed within the granite. This indicates a genetic relationship between the granite and Fe mineralization. The LA-ICP-MS zircon U-Pb dating for the Hutouya granite in this study yields the crystallization age of 231.7 ± 2.1 Ma, which is consistent (within error) with the zircon LA-ICP-MS U-Pb

ages of the monzogranite (230.5 ± 4.2 Ma to 229.5 ± 0.5 Ma; Xi et al., 2010; Xiao et al., 2013) that is associated with the Kendekeke Fe deposit. The LA-ICP-MS zircon U-Pb age (233.5 ± 0.9 Ma) of the Tawenchahanxi granodiorite porphyry in present study is identical (within error) to an $^{40}\text{Ar}-^{39}\text{Ar}$ age (230.7 ± 2.0 Ma; Tian et al., 2013) of phlogopite from magnetite ores, which represents the timing of Fe mineralization. Field relationships show that Fe mineralization and skarns were developed along the contacts between the marble and the granodiorite porphyry at Tawenchahanxi. This suggests that the granodiorite porphyry is genetically associated with the Tawenchahanxi Fe-Cu-Zn deposit. Published data show that the zircon LA-ICP-MS U-Pb age (234.6 ± 0.6 Ma; Gao et al., 2012) for the Galinge quartz monzonite is older than the zircon LA-ICP-MS U-Pb age for the quartz monzodiorite (228.3 ± 0.5 Ma; Gao et al., 2012) at Galinge. This age is identical, within uncertainty, to the $^{40}\text{Ar}-^{39}\text{Ar}$ age (235.8 ± 1.7 Ma; Yu et al., 2015a) of phlogopite from magnetite ores in the Galinge Fe-Zn deposit (Fig. 7). Integrated with the genetic relationship between quartz monzonite and the Galinge deposit (Gao et al., 2012), we suggest that the quartz monzonite is temporally and genetically related to the Galinge Fe-Zn deposit.

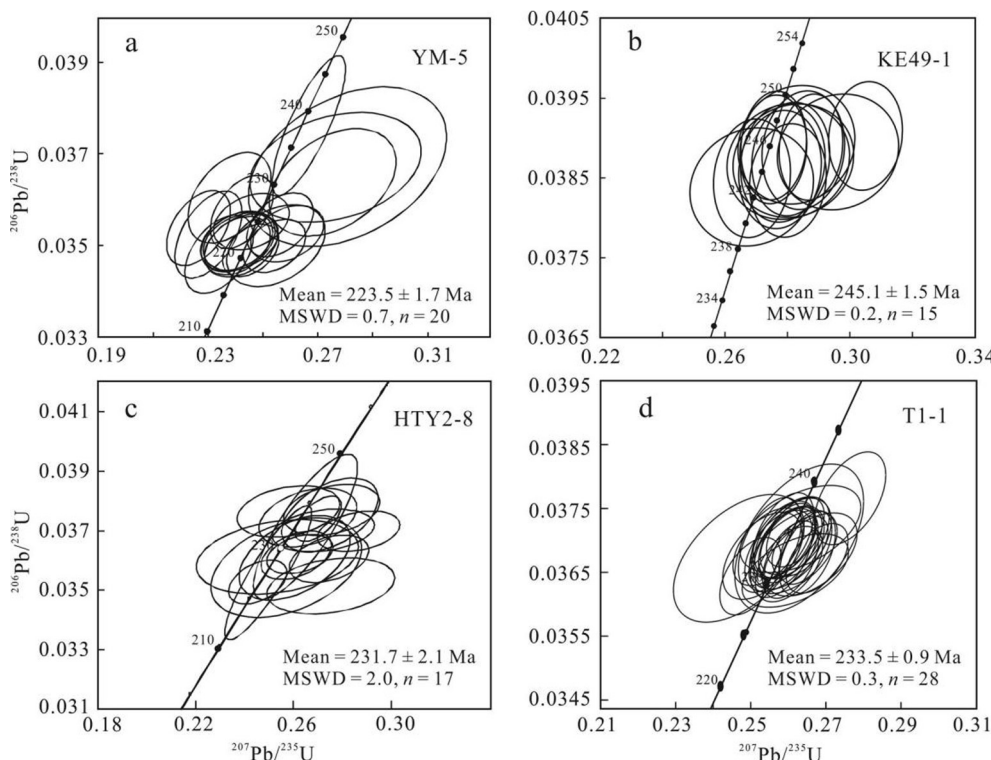


Fig. 4. LA-ICP-MS zircon U-Pb concordia diagrams of (a) Yemaquan monzonite, (b) Kaerqueka granodiorite, (c) Hutouya granite, and (d) Tawenchahanxi granodiorite porphyry.

Table 2
Trace elements of zircons from the Yemiquan monzonite, Kaerqueka granodiorite, Huituya granite, and Tawenchahanxi granodiorite porphyry in the QTGP.

Spot	La	Ce	Pr	Nd	Srn	Eu	Gd	Tb	Dy	Ho	Er	Tm	Yb	Lu	Th	U	Hf	Ta	Ti	Y	Nb	Ce/Nd	Eu/Eu [*]	Ce _N /Ce _N [*]	Ce ⁴⁺ /Ce ³⁺
YM-5 (monzonite)																									
1	0.05	15.4	0.18	2.42	3.86	0.25	20.3	7.09	81.8	30.3	132	28.0	252	47.5	197	375	10160	1.25	8.88	903	1.62	6.39	0.07	23.3	56.4
2	0.07	20.1	0.75	10.5	14.6	0.93	69.1	22.0	243	85.3	349	68.4	591	106	560	711	8363	0.92	12.8	2464	1.61	1.92	0.07	7.97	10.5
3	0.18	21.2	0.49	7.98	12.7	0.75	61.5	19.8	216	76.4	314	62.6	540	97.1	489	629	8686	0.86	9.52	2207	1.50	2.66	0.07	11.8	13.9
4	0.01	12.4	0.07	1.27	2.66	0.25	15.6	5.30	61.5	22.7	98.9	21.3	195	36.4	150	305	9013	0.62	14.9	686	1.29	9.79	0.09	51.3	73.0
5	0.04	12.7	0.12	2.53	5.71	0.43	28.4	9.50	107	37.4	15.9	32.6	286	51.9	177	300	9155	0.53	9.09	1116	0.85	5.03	0.08	29.0	22.5
6	0.01	28.3	0.11	2.18	5.13	0.24	25.8	8.79	103	39.0	16.8	36	326	60.6	526	1012	10428	1.74	9.40	1151	2.24	13.0	0.05	76.4	75.4
7	0.05	41.6	0.16	3.20	6.63	0.31	35.4	12.2	145	54.2	237	49.8	447	82.2	1107	480	10593	2.74	8.26	1627	4.32	13.0	0.05	77.4	89.1
8	0.05	15.2	0.41	6.70	11.3	0.83	51.4	16.0	170	58.8	237	47.2	405	70.7	314	465	8819	0.69	13.2	1747	1.21	2.27	0.09	10.8	8.84
9	0.08	21.6	0.61	8.76	13.5	0.96	73.1	23.1	258	90.9	371	74.1	632	112	804	941	7987	1.20	15.8	2641	2.43	2.47	0.07	10.4	14.4
10	0.08	19.7	0.63	9.37	14.4	0.89	68.5	21.9	241	84.3	346	68.1	589	102	531	707	8322	0.99	12.9	2482	1.63	2.11	0.07	9.22	10.3
11	0.08	14.9	0.23	2.97	4.95	0.39	21.9	7.14	82.0	29.8	129	27.3	249	45.9	263	445	7912	0.78	13.6	899	1.30	5.02	0.10	17.8	32.2
Avg.	0.06	20.3	0.34	5.26	8.68	0.57	42.8	13.9	155.3	55.4	231	46.9	410	73.8	465	579	9040	1.12	11.7	1629	1.82	5.79	0.07	29.6	37.0
KE49-1 (granodiorite)																									
1	0.02	12.8	0.07	0.96	2.22	0.40	12.7	5.05	63.1	26.9	122	33.0	279	65.8	396	842	6676	1.54	2.31	676	3.28	13.4	0.18	52.2	139
2	0.05	11.9	0.05	0.63	1.53	0.19	7.15	2.70	33.6	14.8	65.7	17.8	152	36.2	250	394	5994	0.94	1.88	370	1.54	0.15	50.9	154	154
3	0.14	36.7	0.18	2.65	5.54	1.13	29.7	11.5	155	68.9	315	86.6	753	172	741	1137	12597	2.83	14.8	1741	6.48	13.8	0.21	48.6	167
4	0.02	28.8	0.09	1.41	2.39	0.66	17.6	7.11	92.9	41.9	202	59.7	547	130	607	1284	14258	3.75	5.98	1077	4.91	20.4	0.23	93.4	530
5	0.28	20.5	0.18	1.77	2.59	0.38	12.9	4.26	55.6	23.6	108	28.8	245	56.6	433	661	9249	1.46	3.12	597	2.14	11.6	0.16	21.8	14.3
6	0.03	21.9	0.06	0.93	2.12	0.41	12.3	4.82	60.6	27.5	130	37.6	344	82.9	471	917	14139	2.19	3.95	718	2.78	23.5	0.19	90.1	334
7	0.04	14.4	0.04	0.73	1.61	0.33	9.66	3.60	48.4	22.0	106	29.5	260	63.5	248	439	6316	1.26	4.88	576	2.51	19.6	0.20	78.3	289
8	0.03	13.8	0.05	0.83	2.07	0.21	12.0	5.13	64.4	27.9	126	33.8	279	63.3	469	1098	9074	2.58	1.65	696	3.78	16.6	0.10	67.6	163
Avg.	0.08	20.1	0.09	1.24	2.51	0.46	14.3	5.52	71.7	31.7	147	40.9	357	83.8	452	846	9788	2.07	4.82	806	3.43	17.2	0.18	62.9	240
HTY2-8 (granite)																									
1	0.19	14.8	0.25	2.34	3.73	0.72	17.9	6.61	79.0	32.4	137	35.5	285	64.4	265	418	7649	1.46	4.42	755	3.87	6.31	0.22	14.1	30.4
2	0.21	18.8	0.12	1.38	3.04	0.43	14.7	5.06	60.5	26.0	110	30.6	254	59.1	254	565	10801	1.78	5.94	632	3.60	13.6	0.16	29.4	55.4
3	0.28	14.5	0.24	2.33	2.96	0.65	17.4	6.18	70.6	30.0	127	33.1	264	61.0	229	401	8485	1.09	6.07	719	2.70	6.20	0.22	12.9	45.1
4	0.03	13.8	0.16	2.40	4.56	0.73	22.5	7.80	89.7	36.8	153	38.9	313	70.2	176	348	9377	1.09	44.4	863	2.74	5.73	0.18	25.3	20.5
5	0.01	8.94	0.09	1.32	2.48	0.53	13.5	4.91	58.1	25.3	107	27.4	223	50.8	176	315	5921	0.81	4.51	597	1.62	6.75	0.22	28.8	32.8
6	0.01	17.1	0.13	2.43	4.52	0.92	24.5	8.73	101	41.2	170	41.5	512	71.7	576	718	1437	1.19	9.90	959	3.06	7.06	0.21	40.1	25.3
7	0.03	15.2	0.11	1.83	4.12	0.70	23.3	8.32	95.7	40.3	170	43.4	342	77.1	192	426	10132	1.49	9.54	941	3.96	13.4	0.17	38.9	30.6
8	0.14	13.8	0.16	1.45	2.75	0.17	14.2	5.79	73.0	31.8	139	36.6	294	66.5	436	1108	8072	3.80	2.08	770	8.32	9.49	0.07	20.2	53.8
9	0.01	22.8	0.11	1.89	3.94	0.59	21.9	8.19	96.1	40.3	169	42.2	338	74.8	349	620	8450	2.07	6.71	946	5.57	12.0	0.15	63.0	48.7
10	0.003	24.7	0.12	1.97	5.05	0.61	26.5	9.66	117	48.6	208	55.8	450	101	362	669	13226	2.19	5.72	1130	4.49	12.5	0.13	61.2	44.0
11	0.01	11.3	0.07	1.46	3.39	0.59	16.8	6.10	73.0	30.6	132	33.6	278	62.7	154	320	9437	1.11	8.03	719	2.68	7.73	0.12	46.2	27.2
12	0.003	14.4	0.06	1.08	2.53	0.32	15.1	5.78	72.0	31.3	137	37.1	306	71.3	179	447	9228	1.82	3.58	748	3.70	13.4	0.12	71.7	71.7
13	0.004	22.4	0.09	1.66	3.77	0.45	20.7	7.38	90.5	38.1	168	44.3	362	79.9	350	761	14443	2.18	5.21	921	4.38	13.5	0.12	74.1	56.5
Avg.	0.07	16.3	0.13	1.81	3.60	0.57	19.2	6.96	82.8	34.8	148	38.5	310	69.9	280	536	9415	1.70	8.93	823	3.90	9.43	0.17	40.9	41.7
T1-1 (granodiorite porphyry)																									
1	0.01	16.6	0.12	1.79	3.93	0.86	20.0	6.82	85.5	35.0	172	42.4	444	93.7	524	630	10068	1.43	3.22	1120	1.61	9.32	0.24	42.6	76.9
2	0.001	11.7	0.03	1.85	3.74	0.39	9.41	4.95	21.4	112	29.2	324	71.3	314	742	9363	1.27	4.51	716	1.53	16.7	0.23	12.5	187	
3	0.01	11.7	0.06	1.05	2.30	0.60	12.9	4.82	59.9	24.4	121	29.4	315	66.5	372	674	10230	0.85	1.37	797	0.83	11.2	0.27	57.5	111
4	0.10	16.8	0.18	1.31	2.20	0.31	11.1	4.39	57.0	24.0	125	30.7	317	67.9	458	984	10090	1.73	2.34	12.8	0.16	23.1	179		
5	0.08	12.4	0.12	1.63	2.96	0.63	15.9	5.30	65.7	27.1	135	33.6	368	75.5	353	580	10351	1.11	2.49	883	1.17	7.57	0.22	24.9	81.5
6	0.02	19.6	0.10	2.35	5.64	0.48	34.3	12.5	158	65.1	312	71.2	682	141	789	1242	10565	1.66	1.71	2012	2.38	8.34	0.08	53.8	63.7
7	0.10	13.8	0.03	0.63	1.51	0.31	9.15	3.98	48.9	20.4	104	26.0	253	54.3	370	761	9635	1.58	8.56	686	1.91	21.7	0.20	55.6	245
8	0.03	13.4	0.11	1.70	3.47	0.																			

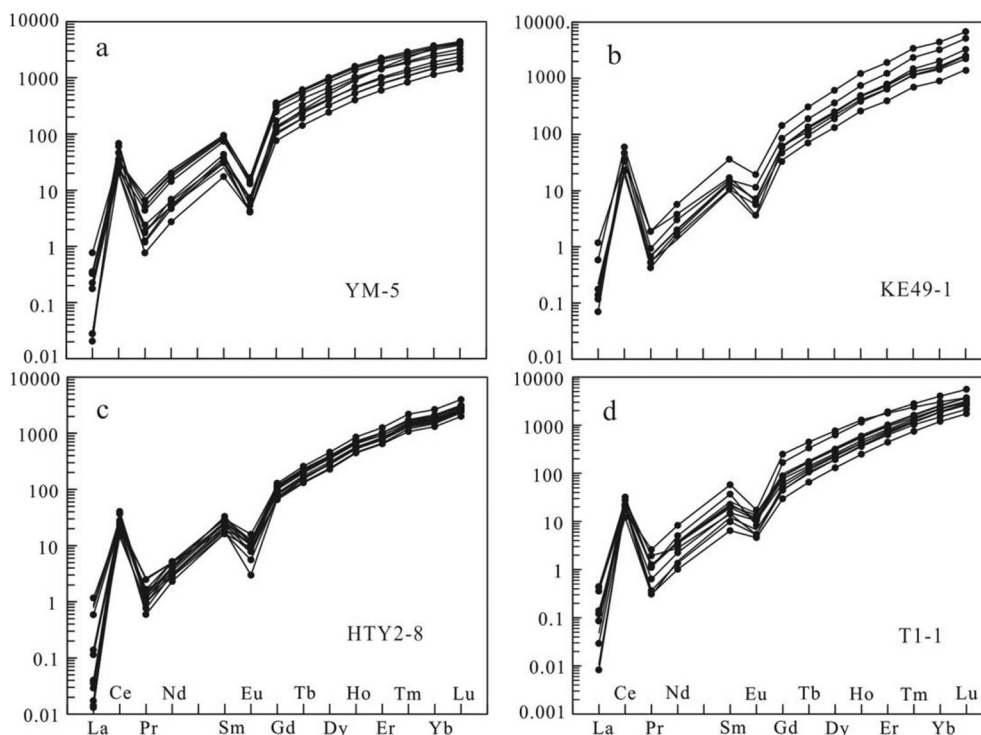


Fig. 5. Chondrite-normalized REE patterns of zircon grains for (a) Yemaquan monzonite, (b) Kaerqueka granodiorite, (c) Hutouya granite, and (d) Tawenchahanxi granodiorite porphyry. The chondrite values are from McDonough and Sun (1995).

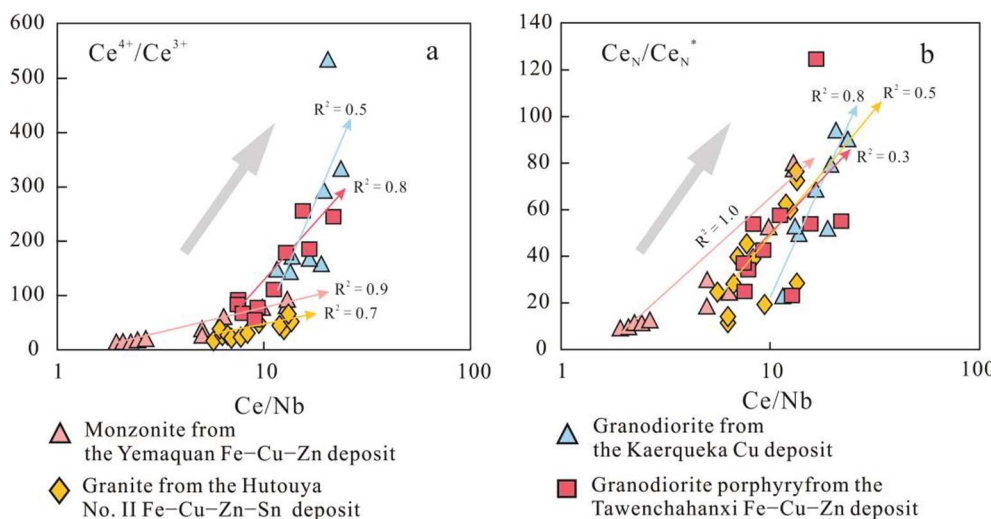


Fig. 6. Diagrams of (a) Ce/Nb vs. $\text{Ce}^{4+}/\text{Ce}^{3+}$ and (b) Ce/Nb vs. $\text{Ce}_N/\text{Ce}_N^*$ for zircons from the Yemaquan monzonite, Kaerqueka granodiorite, Hutouya granite, and Tawenchahanxi granodiorite porphyry. The correlation coefficients (R^2) for regression lines of these rocks are shown.

Based on the zircon U-Pb data of this study and published zircon U-Pb data, and molybdenite Re-Os, and phlogopite $^{40}\text{Ar}-^{39}\text{Ar}$ ages (Xi et al., 2010; Feng et al., 2012; Gao et al., 2012; Gao, 2013; Tian et al., 2013; Xiao et al., 2013; Ma et al., 2015), two discrete suites of the intrusions associated with Fe and Cu skarn deposits in the QTQP have been recognized: (1) Suite 1, 245.1 ± 1.5 Ma granodiorite related to the 245.5 ± 1.6 Ma Cu skarn deposit; (2) Suite 2, 235–224 Ma monzonites, quartz monzonites, granodiorite porphyries, monzogranites, and granites associated with 234–225 Ma Fe skarn deposits.

7.2. Magma source

Zircons in the 245.1 ± 1.5 Ma granodiorite of Suite 1 have $\epsilon\text{Hf}(t)$ values ranging from -11.9 to -2.1 (Fig. 8), similar to those (-9 to -1 ; Wang et al., 2014) of the 245–240 Ma intrusions in the QTQP. Sr-Nd isotopic compositions show that the 245–240 Ma intrusions have $(^{87}\text{Sr}/^{86}\text{Sr})_i$ (0.7111 to 0.7141) and $\epsilon\text{Nd}(t)$ values (-7.4 to -6.3) (Li et al., 2013) similar to those ($(^{87}\text{Sr}/^{86}\text{Sr})_i = 0.7086$ to 0.7150; $\epsilon\text{Nd}(t) = -7.4$ to -3.6) of the Triassic mafic rocks in the EKO, which were derived from enriched lithospheric mantle (Liu et al., 2003; Deng et al., 2004; Xiong et al., 2011; Ding et al., 2014). However, most of the zircon grains in the granodiorite have $\epsilon\text{Hf}(t)$ values lower than those (-2.4 to $+2.9$; Fig. 8) of the Triassic mafic rocks and fall within the field of lower crust in EKO (Fig. 9a). Additionally, most zircons in the granodiorite have two-stage Hf model ages ($T_{2\text{DM}}$) of 1.6 to 1.4 Ga (Table 3), which are obviously younger than the age of the Paleoproterozoic basement in the EKO (ca. 2.1 to 1.7 Ga; Yu et al., 2005; Mo et al., 2007), suggesting juvenile crustal rock as the source for the granodiorite. Recent studies show that crustal growth occurred during Mesoproterozoic time in the EKO, and many Triassic granitic rocks (e.g., Wulonggou) and lavas (e.g., Haishigou) in the region were derived from the partial melting of Mesoproterozoic juvenile mafic lower crust (Ding et al., 2014; Li et al., 2015). Therefore, all these features indicate that Mesoproterozoic juvenile mafic lower crust may have dominated the origin of the granodiorite. However, one zircon in the granodiorite has obviously low $\epsilon\text{Hf}(t)$ values (as low as -11.9) and old

(t) ($= -7.4$ to -3.6) of the Triassic mafic rocks in the EKO, which were derived from enriched lithospheric mantle (Liu et al., 2003; Deng et al., 2004; Xiong et al., 2011; Ding et al., 2014). However, most of the zircon grains in the granodiorite have $\epsilon\text{Hf}(t)$ values lower than those (-2.4 to $+2.9$; Fig. 8) of the Triassic mafic rocks and fall within the field of lower crust in EKO (Fig. 9a). Additionally, most zircons in the granodiorite have two-stage Hf model ages ($T_{2\text{DM}}$) of 1.6 to 1.4 Ga (Table 3), which are obviously younger than the age of the Paleoproterozoic basement in the EKO (ca. 2.1 to 1.7 Ga; Yu et al., 2005; Mo et al., 2007), suggesting juvenile crustal rock as the source for the granodiorite. Recent studies show that crustal growth occurred during Mesoproterozoic time in the EKO, and many Triassic granitic rocks (e.g., Wulonggou) and lavas (e.g., Haishigou) in the region were derived from the partial melting of Mesoproterozoic juvenile mafic lower crust (Ding et al., 2014; Li et al., 2015). Therefore, all these features indicate that Mesoproterozoic juvenile mafic lower crust may have dominated the origin of the granodiorite. However, one zircon in the granodiorite has obviously low $\epsilon\text{Hf}(t)$ values (as low as -11.9) and old

Table 3

Zircon in situ Hf isotopic compositions of the Yemaquan monzonite, Kaerqueka granodiorite, Hutouya granite, and Tawenchahanxi granodiorite porphyry in the QTQP.

Spot	$^{176}\text{Yb}/^{177}\text{Hf}$	2σ	$^{176}\text{Lu}/^{177}\text{Hf}$	2σ	$^{176}\text{Hf}/^{177}\text{Hf}$	2σ	$(^{176}\text{Hf}/^{177}\text{Hf})_i$	$\epsilon\text{Hf(t)}$	T _{1DM} (Ga)	T _{2DM} (Ga)	$f_{\text{Lu/Hf}}$
YM-5 (monzonite)											
1	0.027319	0.000178	0.001018	0.000007	0.282641	0.000016	0.282637	0.3	0.9	1.3	0.9
2	0.030190	0.000112	0.001165	0.000004	0.282652	0.000019	0.282648	0.5	0.9	1.2	0.9
3	0.027039	0.000200	0.001012	0.000007	0.282623	0.000027	0.282618	-0.6	0.9	1.3	0.9
4	0.028357	0.000320	0.001053	0.000012	0.282656	0.000014	0.282652	0.6	0.9	1.2	0.9
5	0.024861	0.000220	0.000921	0.000008	0.282643	0.000033	0.282639	0.4	0.9	1.2	0.9
6	0.017610	0.000219	0.000676	0.000008	0.282599	0.000017	0.282596	-1.3	0.9	1.3	0.9
7	0.023282	0.000123	0.00088	0.000004	0.282603	0.000021	0.282600	-1.2	0.9	1.3	0.9
8	0.032242	0.000371	0.001186	0.000013	0.282649	0.000017	0.282643	0.6	0.9	1.2	0.9
9	0.025848	0.000327	0.001113	0.000015	0.282585	0.000017	0.282580	-1.9	1.0	1.4	1.0
10	0.026921	0.000517	0.001015	0.000019	0.282643	0.000017	0.282639	0.2	0.9	1.3	0.9
11	0.037590	0.000355	0.001412	0.000012	0.282659	0.000016	0.282653	0.8	0.9	1.2	0.9
12	0.043196	0.000334	0.001597	0.000012	0.282642	0.000019	0.282635	0.0	0.9	1.3	0.9
13	0.014811	0.000142	0.000580	0.000006	0.282673	0.000015	0.282671	1.3	0.8	1.2	0.8
14	0.020941	0.000171	0.000814	0.000007	0.282645	0.000013	0.282642	0.4	0.9	1.2	0.9
15	0.055606	0.000364	0.002067	0.000013	0.282683	0.000018	0.282674	1.4	0.8	1.2	0.8
16	0.041976	0.000249	0.001551	0.000009	0.282684	0.000018	0.282678	1.6	0.8	1.2	0.8
17	0.033785	0.000015	0.001226	0.000000	0.282633	0.000018	0.282628	-0.2	0.9	1.3	0.9
18	0.055813	0.000317	0.002073	0.000012	0.282621	0.000020	0.282612	-0.7	0.9	1.3	0.9
19	0.023868	0.000100	0.000905	0.000004	0.282653	0.000016	0.282649	0.6	0.9	1.2	0.9
20	0.019595	0.000281	0.000745	0.000010	0.282609	0.000017	0.282606	-0.7	0.9	1.3	0.9
KE49-1 (granodiorite)											
1	0.029997	0.000176	0.001250	0.000007	0.282516	0.000017	0.282511	-3.8	1.0	1.5	-0.96
2	0.031694	0.001500	0.001328	0.000059	0.282515	0.000016	0.282509	-3.9	1.1	1.5	-0.96
3	0.026194	0.000284	0.001108	0.000012	0.282548	0.000022	0.282542	-2.7	1.0	1.4	-0.97
4	0.020569	0.000044	0.000918	0.000001	0.282560	0.000016	0.282556	-2.2	1.0	1.4	-0.97
5	0.023212	0.000127	0.001013	0.000005	0.282522	0.000015	0.282517	-3.6	1.0	1.5	-0.97
6	0.027816	0.000127	0.001176	0.000005	0.282534	0.000018	0.282529	-3.4	1.0	1.5	-0.96
7	0.025479	0.000231	0.001120	0.000010	0.282519	0.000017	0.282514	-3.8	1.0	1.5	-0.97
8	0.049370	0.000229	0.001906	0.000009	0.282512	0.000017	0.282503	-4.1	1.1	1.5	-0.94
9	0.030141	0.000473	0.001239	0.000018	0.282523	0.000016	0.282517	-3.7	1.0	1.5	-0.96
10	0.032787	0.000382	0.001368	0.000016	0.282291	0.000015	0.282285	-11.9	1.4	2.0	-0.96
11	0.024373	0.000376	0.001070	0.000016	0.282518	0.000016	0.282513	-3.8	1.0	1.5	-0.97
12	0.020916	0.000235	0.000912	0.000009	0.282543	0.000013	0.282539	-2.8	1.0	1.5	-0.97
13	0.017599	0.000114	0.000786	0.000005	0.282540	0.000017	0.282536	-3.1	1.0	1.5	-0.98
14	0.031059	0.000131	0.001287	0.000005	0.282566	0.000017	0.282560	-2.1	1.0	1.4	-0.96
15	0.019281	0.000100	0.000863	0.000005	0.282497	0.000018	0.282493	-4.5	1.1	1.6	-0.97
HTY2-8 (granite)											
1	0.021341	0.000221	0.000890	0.000009	0.282616	0.000017	0.282612	-0.5	0.9	1.3	-0.97
2	0.033872	0.000105	0.001374	0.000004	0.282616	0.000015	0.282610	-0.7	0.9	1.3	-0.96
3	0.023855	0.000120	0.001002	0.000005	0.282628	0.000016	0.282624	-0.2	0.9	1.3	-0.97
4	0.016320	0.000121	0.000709	0.000005	0.282544	0.000014	0.282541	-3.1	1.0	1.5	-0.98
5	0.094268	0.001070	0.003659	0.000032	0.282607	0.000016	0.282591	-1.3	1.0	1.4	-0.89
6	0.016905	0.000049	0.000720	0.000003	0.282641	0.000016	0.282638	0.3	0.9	1.2	-0.98
7	0.026890	0.000197	0.001118	0.000009	0.282663	0.000017	0.282658	1.1	0.8	1.2	-0.97
8	0.064056	0.000778	0.002407	0.000021	0.282652	0.000020	0.282642	0.5	0.9	1.2	-0.93
9	0.018456	0.000120	0.000752	0.000004	0.282614	0.000017	0.282610	-0.6	0.9	1.3	-0.98
10	0.022406	0.000155	0.000940	0.000006	0.282615	0.000017	0.282611	-0.6	0.9	1.3	-0.97
11	0.043402	0.000268	0.001648	0.000009	0.282581	0.000020	0.282574	-1.9	1.0	1.4	-0.95
12	0.020936	0.000060	0.000873	0.000002	0.282577	0.000018	0.282573	-2.0	1.0	1.4	-0.97
13	0.030377	0.000092	0.001266	0.000003	0.282622	0.000016	0.282617	-0.4	0.9	1.3	-0.96
14	0.016300	0.000123	0.000682	0.000005	0.282622	0.000016	0.282619	-0.4	0.9	1.3	-0.98
15	0.016316	0.000171	0.000683	0.000007	0.282612	0.000018	0.282609	-0.7	0.9	1.3	-0.98
T1-1 (granodioriteporphyry)											
1	0.020099	0.000115	0.00087	0.000005	0.282561	0.000015	0.282557	-2.4	1.0	1.4	-0.97
2	0.013407	0.000092	0.000598	0.000004	0.282551	0.000014	0.282548	-2.8	1.0	1.4	-0.98
3	0.017398	0.000229	0.000781	0.000009	0.282532	0.000014	0.282529	-3.5	1.0	1.5	-0.98
4	0.014571	0.000161	0.000643	0.000006	0.282526	0.000016	0.282523	-3.7	1.0	1.5	-0.98
5	0.023702	0.000439	0.001018	0.000018	0.282573	0.000015	0.282569	-2.0	1.0	1.4	-0.97
6	0.017541	0.000361	0.000777	0.000017	0.282593	0.000015	0.282589	-1.3	0.9	1.4	-0.98
7	0.019900	0.000251	0.000853	0.000010	0.282517	0.000014	0.282513	-4.1	1.0	1.5	-0.97
8	0.018399	0.000156	0.000808	0.000007	0.282581	0.000017	0.282577	-1.8	1.0	1.4	-0.98
9	0.017931	0.000088	0.000825	0.000005	0.282568	0.000016	0.282565	-2.2	1.0	1.4	-0.98
10	0.027538	0.000241	0.001171	0.000009	0.282529	0.000014	0.282524	-3.7	1.0	1.5	-0.96
11	0.019195	0.000364	0.000852	0.000016	0.282546	0.000015	0.282542	-3.0	1.0	1.5	-0.97
12	0.018513	0.000169	0.000801	0.000008	0.282570	0.000015	0.282567	-2.1	1.0	1.4	-0.98
13	0.021843	0.000151	0.001006	0.000007	0.282536	0.000016	0.282532	-3.4	1.0	1.5	-0.97
14	0.019573	0.000118	0.000874	0.000005	0.282571	0.000015	0.282567	-2.1	1.0	1.4	-0.97
15	0.016822	0.000053	0.000750	0.000020	0.282555	0.000015	0.282551	-2.7	1.0	1.4	-0.98
16	0.030764	0.000107	0.001259	0.000037	0.282557	0.000015	0.282552	-2.6	1.0	1.4	-0.96
17	0.022928	0.000326	0.000985	0.000012	0.282533	0.000015	0.282529	-3.5	1.0	1.5	-0.97

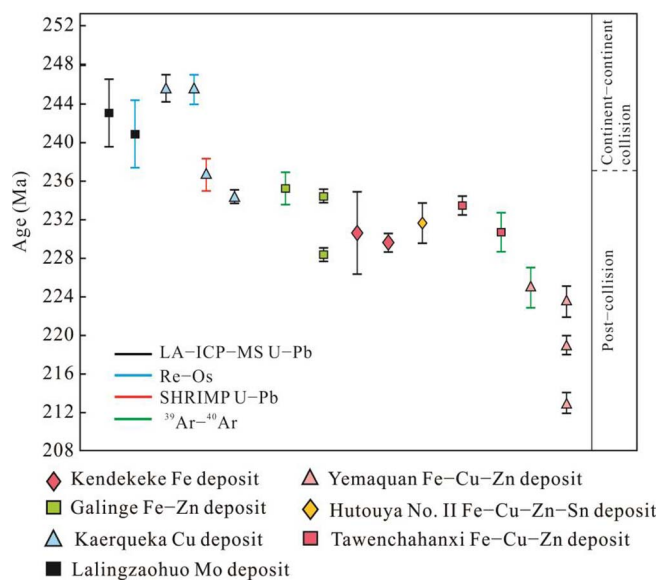


Fig. 7. Age distribution of the Fe and Cu skarn deposits for ores and intrusions from the QTQP. The isotopic age data sources are as follows: Kendekeke (Xi et al., 2010; Xiao et al., 2013), Yemaquan (Gao et al., 2014; Ma et al., 2015; this study), Galinge (Gao et al., 2012; Yu et al., 2015a), Hutouya (this study), Kaerqueka (Wang et al., 2009; Gao, 2013; Gao et al., 2015; this study), Tawenchahanxi (Tian et al., 2013; this study), and Lalingzaohuo (Chen et al., 2013; Wang et al., 2013).

$T_{2\text{DM}}$ ages (as old as 2.0 Ga), reflecting the mixing of mantle and ancient lower-crustal materials (Griffin et al., 2002; Kemp et al., 2007; Shaw and Flood, 2009). Given these features, we conclude that the rock of Suite 1 was dominantly derived from partial melting of Mesoproterozoic juvenile mafic lower crust, together with the involvement of minor ancient lower-crustal components during the evolution of the magma.

Most zircons in the intrusions of Suite 2 have $\epsilon\text{Hf(t)}$ values similar to those of the Triassic mafic rocks in the EKO (Fig. 8), which were derived from enriched lithospheric mantle (Xiong et al., 2011; Hu et al., 2015; Xia et al., 2015b). The rocks of Suite 2 have Hf isotopic compositions similar to those of the 235–213 Ma granitic rocks ($\epsilon\text{Hf(t)} = -6.3$ to $+5.9$; Yao, 2015; Fig. 8) in the QTQP. The Sr-Nd isotopic compositions show that the 235–213 Ma granitic rocks have $(^{87}\text{Sr}/^{86}\text{Sr})_i$ values (0.7091 to 0.7139) and $\epsilon\text{Nd(t)}$ values (-6.6 to -0.1) (Wu et al., 2011; Feng et al., 2012; Yao, 2015; Yao et al., 2015c) similar to those of the Triassic mafic rocks ($(^{87}\text{Sr}/^{86}\text{Sr})_i = 0.7086$ to 0.7150 ; $\epsilon\text{Nd(t)} = -7.4$ to -3.6) in the EKO, which were derived from enriched lithospheric mantle (Liu et al., 2003; Deng et al., 2004; Xiong et al., 2011; Ding et al., 2014). This indicates that the rocks of Suite 2 were probably derived from an enriched mantle source. However, most of zircons in the rocks of Suite 2 have positive $\epsilon\text{Hf(t)}$ values (Figs. 8 and 9a). Some zircons in these rocks have higher $\epsilon\text{Hf(t)}$ values than those of the Triassic mafic rocks in the EKO (Fig. 8). Furthermore, their two-stage Hf model ages ($T_{2\text{DM}} = 1.6$ to 0.9 Ga; Gao et al., 2012; Xiao et al., 2013; Table 3) are obviously younger than ages of the Paleoproterozoic basement in the EKO (ca. 2.1 to 1.7 Ga; Yu et al., 2005; Mo et al., 2007). All these features suggest that the partial melting of Mesoproterozoic juvenile mafic crust with a contribution of depleted mantle materials into the magma source may be responsible for the generation of these rocks (Griffin et al., 2002; Wong et al., 2009). Therefore, considering Sr-Nd-Hf isotopic compositions, we argue that the intrusions of Suite 2 were dominantly derived from partial melting of the Mesoproterozoic juvenile crustal rocks, together with the involvement of various amounts of depleted mantle components during the evolution of the magma.

7.3. Relationship between magma sources and Fe and Cu skarn deposits

Compared with the intrusion of Suite 1, the rocks of Suite 2 have relatively higher $\epsilon\text{Hf(t)}$ values (Figs. 8 and 9a), indicating that intrusions associated with Fe skarn deposits have more mantle materials in their magma sources than the intrusion related to Cu skarn deposit. As mentioned above, some Fe skarn deposits in the QTQP not only contain magnetite, but also contain economic concentrations of Cu and Zn (e.g., the Yemaquan Fe-Cu-Zn, Galinge Fe-Zn, Tawenchahanxi Fe-Cu-Zn and Hutouya No. II Fe-Cu-Zn-Sn deposits; Zhang et al., 2013; Yu et al., 2015a; Zuo et al., 2015). Zircon Hf isotopic compositions (Figs. 8 and 9a) show that the monzogranite associated with the Kendekeke Fe deposit has higher $\epsilon\text{Hf(t)}$ values ($+0.8$ to $+5.9$; Xiao et al., 2013) than those (-5.1 to $+1.7$; Gao et al., 2012; this study) of the intrusions related to the Yemaquan, Tawenchahanxi, Galinge, and Hutouya No. II deposits, implying that the intrusions associated with the Fe skarn deposits that contain significant amounts of Cu and Zn, involve more crustal materials in their magma sources. Compared with Yemaquan monzonite, Galinge quartz monzonite, Tawenchahanxi granodiorite porphyry, and Hutouya granite, the granodiorite associated with the Kaerqueka Cu deposit has relatively lower $\epsilon\text{Hf(t)}$ values, indicating more crustal components were involved in the magma source. These features suggest that the $\epsilon\text{Hf(t)}$ values of the intrusions associated with Fe and Cu skarn deposits in the QTQP decrease from the Kendekeke Fe deposit to Kaerqueka Cu deposit (Figs. 8 and 9a), reflecting a negative correlation between mantle component in the magma sources of these intrusions and the content of Cu and Zn in these deposits. Meinert (1995) compiled the major and trace element geochemical data for plutons related to skarn deposits worldwide, and suggested that the mantle materials involved in the magma sources of intrusions associated with various skarn types appear to decline follow this trend in the order: Fe, Au, Cu, Zn, W, Mo, and Sn. Therefore, based on zircon Hf isotopic compositions of the intrusions associated with Fe and Cu skarn deposits in the QTQP, we argue that different proportions of mantle and crustal materials in their magma sources play an essential role in controlling differences between Fe and Cu skarn deposits.

Recent studies indicate that the QTQP underwent Middle Triassic continent-continent collision (~ 237 Ma; Mo et al., 2007; Huang et al., 2014; Xia et al., 2015b; Yu et al., 2017) and Late Triassic post-collision (237–204 Ma; Feng et al., 2012; Yu et al., 2015b) processes, which were induced by the closure of the Paleo-Tethys Ocean (Mo et al., 2007; Qiu and Deng, 2016). Recent Nd-Hf isotopic data show that the 235–213 Ma intrusions ($\epsilon\text{Nd(t)} = -6.6$ to -0.1 ; Wu et al., 2011; Feng et al., 2012; Gao et al., 2015; Yao, 2015; Yao et al., 2015c; $\epsilon\text{Hf(t)} = -6.3$ to $+5.9$; Wu et al., 2011; Gao et al., 2012, 2014; Gao, 2013; Xiao et al., 2013; Yu, 2013; Yao, 2015) formed with a greater contribution of mantle components than those of the 245–240 Ma intrusions ($\epsilon\text{Nd(t)} = -7.4$ to -6.3 ; Li et al., 2013; $\epsilon\text{Hf(t)} = -9$ to -1 ; Wang et al., 2014; Fig. 9b-c) in the QTQP, reflecting lithospheric extension and underplating of mantle-derived basaltic melts that occurred during the Late Triassic (Mo et al., 2007). Molybdenite Re-Os isotopic compositions of the Cu, Mo, and Zn skarn deposits in the QTQP demonstrated that the molybdenites with the model ages of 245–240 Ma exhibit obviously lower Re contents (2 ppm to 87 ppm) than those of molybdenites (24 ppm to 365 ppm) with model ages of 237–214 Ma (Fig. 9d; Feng et al., 2009, 2011; Gao, 2013; Wang et al., 2013). Mao et al. (1999) and Stein et al. (2001) suggested that molybdenites from deposits with a mantle component have significantly higher Re contents than those derived from a crustal source. This indicates that more mantle materials were involved in the metallogenetic system of the Late Triassic, which shares a similar source with the 237–214 Ma intrusions within the QTQP. Sulfur isotopic compositions show that sulfides (such as chalcopyrite, pyrrhotite, galena, sphalerite, molybdenite, and pyrite) during the quartz-sulfide stage from the Triassic Fe, Cu, Mo, and Zn skarn deposits in the QTQP have $\delta^{34}\text{S}$ values ($-3.0\text{\textperthousand}$ to $+9.0\text{\textperthousand}$; reviewed by Yao, 2015) similar to most skarn deposits worldwide (e.g.,

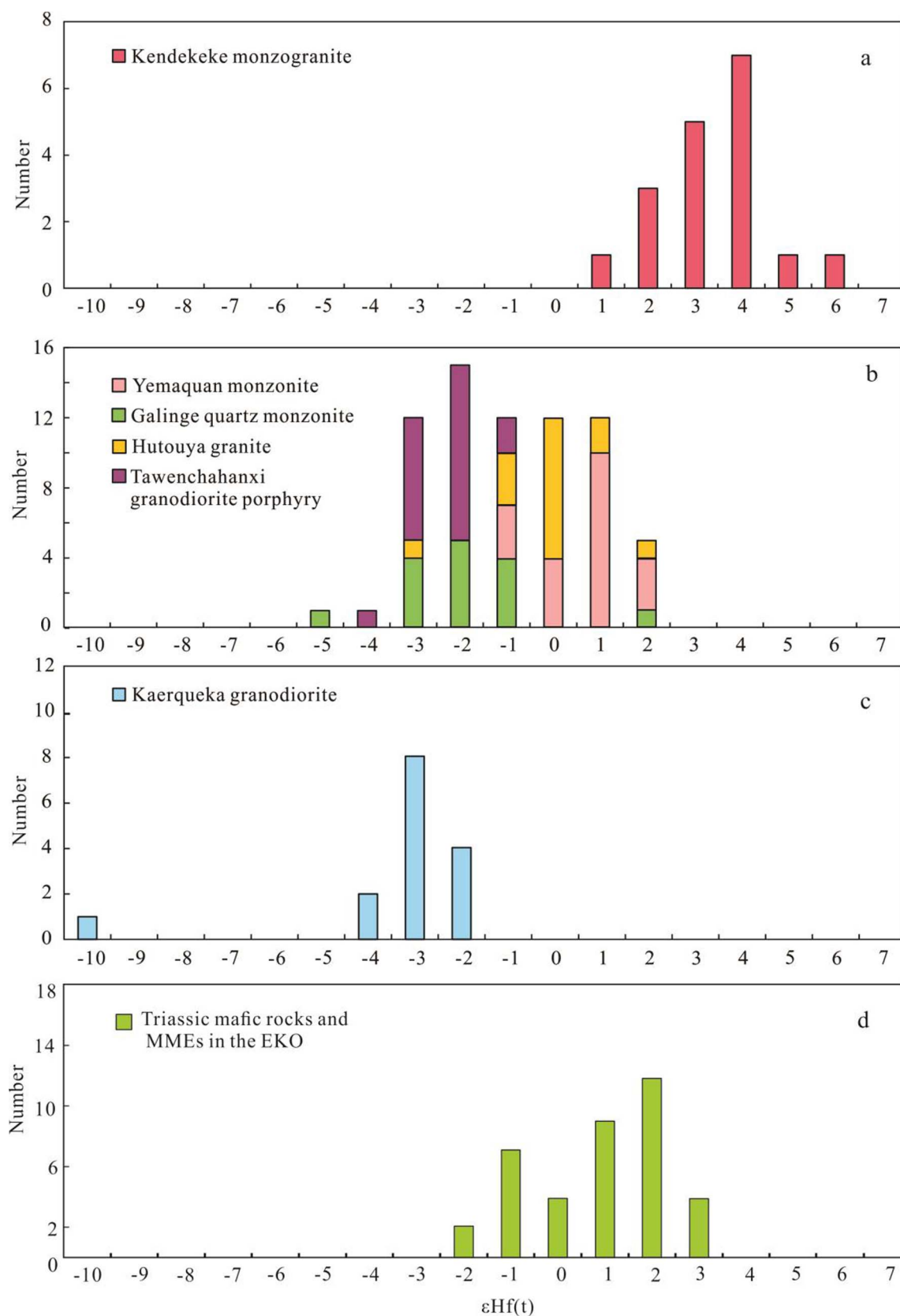


Fig. 8. Histogram of zircon $\epsilon\text{Hf}(t)$ values of intrusions associated with the Fe and Cu skarn deposits in the QTQP. The Hf isotopic data of the Kendekeke monzogranite and Galinge quartz monzonite are from Gao et al. (2012) and Xiao et al. (2013), respectively. The Hf isotopes of mafic rocks in the EKO are from Xiong et al. (2011) and our unpublished data.

Bowman, 1998; Yang and Lee, 2011; Zhao et al., 2012), indicating that magmatic fluids as the main source for these deposits. Therefore, all these evidence suggests that: (1) the tectonic transition from syn-

collision to post-collision settings was responsible for the contribution of mantle component into the magma sources of Late Triassic intrusions; (2) mantle materials involved in the metallogenesis system were

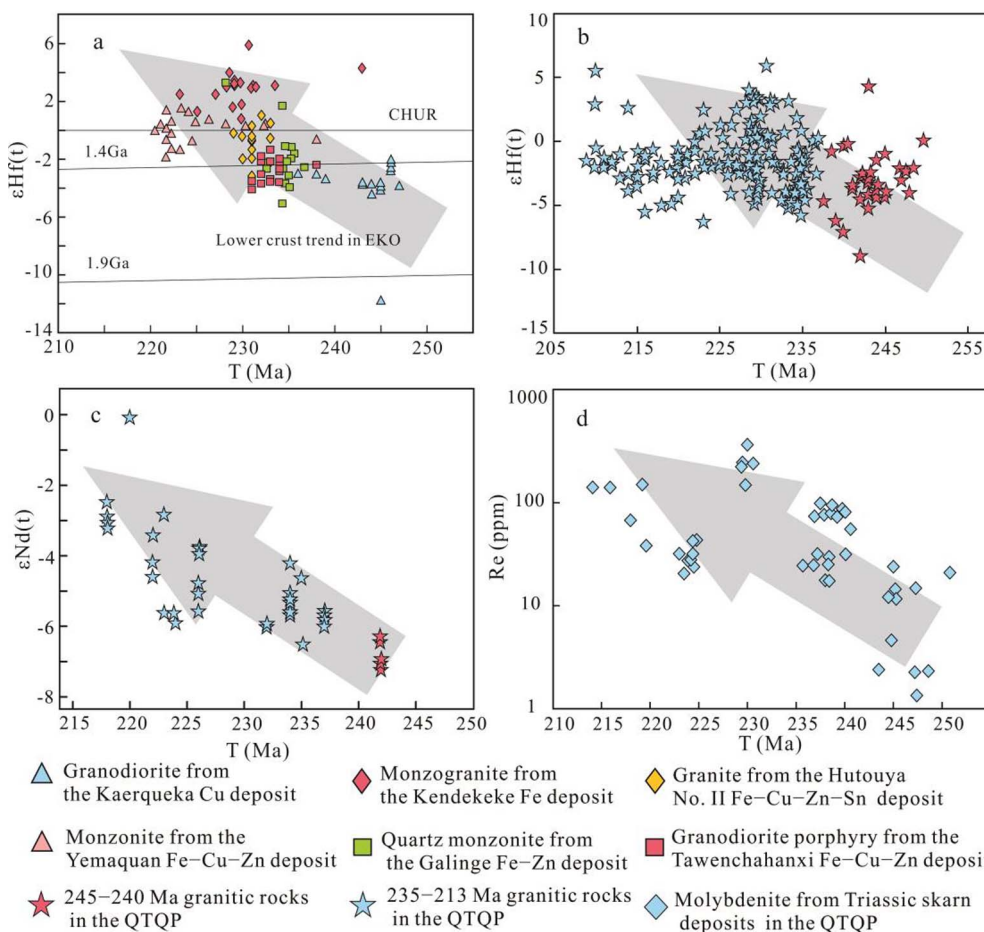


Fig. 9. (a) Plot of the zircon Hf isotopes vs. zircon U–Pb ages for the intrusions associated with Fe and Cu skarn deposits; (b) Plot of the zircon Hf isotopes vs. zircon U–Pb ages for Triassic intrusions in the QTQP; (c) Plot of whole-rocks Nd isotopes vs. zircon U–Pb ages for Triassic intrusions in the QTQP; (d) Plots of Re–Os isotopic model ages vs. Re contents for molybdenites from Triassic skarn deposits in the QTQP. Zircon U–Pb and Hf isotopic data of Triassic igneous rocks in the QTQP are from Wu et al. (2011), Gao et al. (2012, 2014), Gao (2013), Xiao et al. (2013), Yu (2013), Wang et al. (2014) and Yao (2015). Whole-rock Nd isotopes of Triassic igneous rocks in the QTQP are from Wu et al. (2011), Feng et al. (2012), Li et al. (2013) and Yao (2015). Re–Os isotopic compositions of molybdenites from the Triassic skarn deposits in the QTQP are from Feng et al. (2009, 2011), Gao (2013) and Wang et al. (2013).

derived from the magma sources of the mineralization-related intrusions. As mentioned above, the Fe skarn deposits are associated with the granitic rocks of Suite 2 (235–224 Ma) and the Cu skarn deposit is related to 245.1 ± 1.5 Ma granodiorite (Fig. 7). This suggests that the Fe and Cu skarn deposits in the QTQP are associated with different magmatism and geological settings, and the Fe skarn deposits were associated with underplating of mantle-derived basaltic melts induced by lithospheric extension. Thus, all these features indicate that different proportions of mantle and crustal components in the magma sources is one of the most critical factors controlling differences in metal association between Fe and Cu skarn deposits.

Previous studies indicate that the magma source not only provides amounts of metals, but also optimum conditions (e.g., water, oxidation, pressure, temperature and volatile) (e.g., Meinert et al., 2005). Therefore, different compositions of magma sources can affect metal contents and optimum conditions, to a great extent, leading to differences in metal association among various skarn deposits. Many studies indicated that Fe mainly comes from the mantle (e.g., Meinert et al., 2005), and thus the involvement of mantle materials can elevate iron contents of the magma source, favoring the formation of Fe skarn deposits. As mentioned above, almost all the Fe skarn deposits in the QTQP were associated with the Late Triassic intrusions, which contain more mantle components than the Middle Triassic igneous rocks (Fig. 9b–c). This indicates that the involvement of mantle components in the magma sources might play an important role in the formation of these Fe skarn deposits.

Oxygen fugacity is one of the most important conditions that control the enrichment of Fe and Cu during magma evolution (e.g., Reynolds, 1985; Meinert et al., 2005; Pang et al., 2008; Sillitoe, 2010; Richards, 2015; Sun et al., 2015). Relatively low oxygen fugacity can suppress the crystallization of Fe–Ti oxides and promote the crystallization of Fe-

poor silicate minerals (e.g., olivine and plagioclase) during magma evolution, leading to the enrichment of Fe in residual magma, which is favorable for the formation of Fe mineralization (e.g., Reynolds, 1985). In contrast, high oxygen fugacity makes chalcophile elements tend to remain in the melt, and thereby increases Cu concentrations in evolved magmas, favoring Cu mineralization (e.g., Richards, 2015; Sun et al., 2015; Zhang et al., 2017). Zircon $\text{Ce}^{4+}/\text{Ce}^{3+}$ and Ce/Nd ratios (Fig. 6; Table 2) indicate that the magmas of intrusions associated with Fe skarn deposits are relatively less oxidized than that of rock associated with the Cu skarn deposit in the study area. This is also supported by the major element features of these intrusions, which is consistent with intrusive rocks related to Fe and Cu skarn deposits worldwide (e.g., Meinert et al., 2005; Fig. 2e). Although the cause of this phenomenon can be associated with many factors, one of the most important factors may be different proportions of mantle and crustal components in the magma source. As shown in Figs. 6 and 10, the zircon $\text{Ce}^{4+}/\text{Ce}^{3+}$ and Ce/Nd ratios decrease from the Kaerqueka granodiorite, to Tawenchahanxi granodiorite porphyry, to Hutouya granite, and then to Yemaquan monzonite. However, the average zircon $\epsilon\text{Hf(t)}$ values of these intrusions are -4.0 , -2.8 , -0.7 , and $+0.1$, respectively (Fig. 10; Table 3). The decreasing trends of $\text{Ce}^{4+}/\text{Ce}^{3+}$ and Ce/Nd ratios are contrary to that for the $\epsilon\text{Hf(t)}$ values of corresponding rocks (Fig. 10), reflecting a positive correlation between crustal component in the magma source and oxygen fugacity of the magma. Previous studies indicate that the involvement of a crustal component can elevate the oxygen fugacity of magma, if it contain water and oxidized materials (e.g., Fe^{3+} , C^{4+} , and S^{6+}) (e.g., Lee et al., 2005; Evans et al., 2012). For example, the juvenile arc lower crust material may elevate the oxygen fugacity of the magma, because it can inherit the arc magma characteristics of high oxidation state (McInnes and Cameron, 1994; Mungall, 2002; Li et al., 2011). Therefore, considering zircon Hf

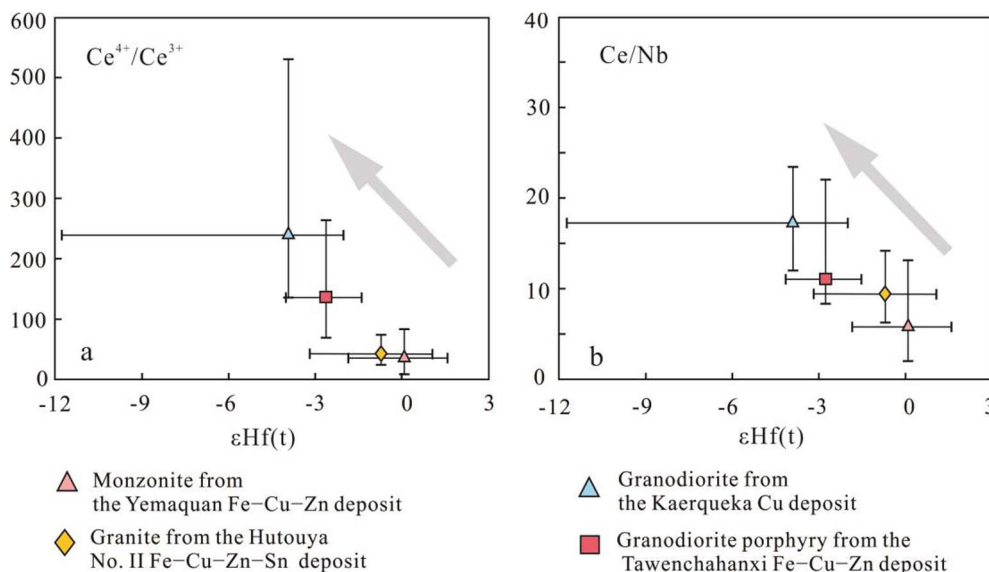


Fig. 10. Plots of (a) $\epsilon\text{Hf(t)}$ vs. $\text{Ce}^{4+}/\text{Ce}^{3+}$ and (b) $\epsilon\text{Hf(t)}$ vs. Ce/Nb for zircons from the Yemaquan monzonite, Kaerqueka granodiorite, Hutouya granite, and Tawenchahanxi granodiorite porphyry.

isotopic and trace element compositions, we argue that a high oxygen fugacity of magma associated with Cu skarn deposit can be most possibly attributed to more crustal materials in the magma source in the QTQP. Integrated zircon U-Pb isotopic, trace element, and Hf isotopic data of this study, with previously published mineralogy and isotopes, indicate that different proportions of mantle and crustal materials in the magma sources may affect oxygen fugacity and Fe contents of the magmas, which possibly leads to the variations in metal associations between Fe and Cu skarn deposits in the QTQP.

8. Conclusions

- (1) Two discrete suites of the intrusions associated with Fe and Cu skarn deposits in the QTQP have been recognized: (1) 245.1 ± 1.5 Ma granodiorite associated with a Cu skarn deposit; (2) 235–224 Ma quartz monzonite, monzonite, granodiorite porphyry, monzogranite, and granite associated with Fe skarn deposits.
- (2) The intrusions of Suite 1 and 2 were derived from the partial melting of Mesoproterozoic juvenile mafic lower crust, and the intrusion of Suite 1 has a greater contribution of crustal components compared to the rocks of Suite 2. The intrusions of Suite 1 are relatively more oxidized than the rocks of Suite 2, which is caused by the involvement of crustal components in the magma source.
- (3) The geological, geochronological and geochemical evidence indicates that different proportions of mantle and crustal materials in the magma sources may affect oxygen fugacity and Fe contents of the magmas, controlling differences between Fe and Cu skarn deposits.

Acknowledgements

This study was jointly supported by National Key R & D Program of China (Grant no. 2017YFC0601506) and the Geological Survey Project of China Geological Survey (DD20160052, 12120115037101). The manuscript benefited greatly from the constructive comments of Prof. Noel White, Franco Pirajno, Olga Plotinskaya, Taoifa Zhou, David Lentz, Guiqing Xie, and two anonymous reviewers. We also thank Tianzhu Ye, Wan Jiang, Xinyou Zhu, Hui Chen, Kejun Hou, Chunli Guo, Qian Wang, Wei Zhang, Xiaoxiong Li, Ming Kong and Han Zhang for assistance during this research and for constructive discussions. Dongsheng Li, Shuyue He, Wei Dai, Longsheng Bai and other local geologists from the Third Institution of Qinghai Geological Mineral Prospecting, China, are thanked for assistance during fieldwork.

Appendix A. Supplementary data

Supplementary data associated with this article can be found, in the online version, at <http://dx.doi.org/10.1016/j.oregeorev.2017.09.017>.

References

- Belousova, E.A., Griffin, W.L., O'Reilly, S., 2006. Zircon crystal morphology, trace element signatures and Hf isotope composition as a tool for petrogenetic modeling: examples from eastern Australian granitoids. *J. Petrol.* 47, 329–353.
- Bowman, J.R., 1998. Stable isotope systematic of skarns. In: Lentz, D.R. (Ed.), Mineralized Intrusion-related Skarn Systems. Mineralogical Association of Canada Short Course Series 26, pp. 99–145.
- Chappell, B.W., White, A., 2001. Two contrasting granite types: 25 years later. *Aust. J. Earth Sci.* 48, 489–499.
- Chelle-Michou, C., Chiaradia, M., Ovtcharova, M., Ulianov, A., Wotzlaw, J.F., 2014. Zircon petrochronology reveals the temporal link between porphyry systems and the magmatic evolution of their hidden plutonic roots (the Eocene Corocochayco deposit, Peru). *Lithos* 198, 129–140.
- Chen, J., Xie, Z.Y., Li, B., Li, S.P., Tan, S.X., Ren, H., Zhang, Q.M., 2013. Geological and geochemical characteristics of the ore-bearing intrusions from the Lalingzaohuo Mo polymetallic deposit and its metallogenetic significance. *Geol. Explor.* 49, 813–824 (in Chinese with English abstract).
- Chu, N.C., Taylor, R.N., Chavagnac, V., Nesbitt, R.W., Boella, R.M., Milton, J.A., German, C.R., Bayon, G., Burton, K., 2002. Hf isotope ratio analysis using multi-collector inductively coupled plasma mass spectrometry: an evaluation of isobaric interference corrections. *J. Anal. At. Spectrom.* 17, 1567–1574.
- Deng, J.F., Luo, Z.H., Su, S.G., Mo, X.X., Yu, B.S., Lai, X.Y., Chen, H.W., 2004. Petrogenesis, Tectonic Setting and Mineralization. Geological Publishing House, Beijing pp. 242–276 (in Chinese).
- Ding, Q.F., Jiang, S.Y., Sun, F.Y., 2014. Zircon U-Pb geochronology, geochemical and Sr-Nd-Hf isotopic compositions of the Triassic granite and diorite dikes from the Wulongguo mining area in the Eastern Kunlun Orogen, NW China: petrogenesis and tectonic implications. *Lithos* 205, 266–283.
- Einaudi, M.T., Meinert, L.D., Newberry, R.J., 1981. Skarn deposits. *Economic Geology*. 75th Anniversary Volume, pp. 317–391.
- Einaudi, M.T., Burt, D.M., 1982. Introduction terminology, classification and composition of skarn deposits. *Econ. Geol.* 77, 745–754.
- Evans, K.A., Elburg, M.A., Kamenetsky, V.S., 2012. Oxidation state of subarc mantle. *Geology* 40 (9), 783–786.
- Feng, C.Y., Li, D.S., Qu, W.J., Du, A.D., Wang, S., Su, S.S., Jiang, J.H., 2009. Copper-Molybdenum deposit of Qimantage Mountain in Qinghai Province and its geological significance. *Rock Miner. Anal.* 28 (3), 223–227 (in Chinese with English abstract).
- Feng, C.Y., Wang, X.P., Shu, X.F., Zhang, A.K., Xiao, Y., Liu, J.N., Ma, S.C., Li, G.C., Li, D.X., 2011. Isotopic chronology of the Hutouya skarn lead-zinc polymetallic ore district in Qimantage area of Qinghai Province and its geological significance. *J. Jilin University (Earth Science Edition)* 41, 1806–1817 (in Chinese with English abstract).
- Feng, C.Y., Wang, S., Li, G.C., Ma, S.C., Li, D.S., 2012. Middle to late Triassic granitoids in the Qimantage area, Qinghai Province, China: chronology, geochemistry and metallogenetic significances. *Acta Petrologica Sinica* 28, 665–678 (in Chinese with English abstract).
- Ferry, J.M., Watson, E.B., 2007. New thermodynamic models and revised calibrations for the Ti-in-zircon and Zr-in-rutile thermometers. *Contrib. Miner. Petrol.* 154, 429–437.
- Gao, Y.B., Li, W.Y., Ma, X.G., Zhang, Z.W., Tang, Q.Y., 2012. Genesis, geochronology and Hf isotopic compositions of the magmatic rocks in Galinge iron deposit, eastern

- Kunlun. *J. Lanzhou University (Natural Sciences)* 48, 36–47 (in Chinese with English abstract).
- Gao, Y.B., 2013. The intermediate-acid intrusive magmatism and mineralization in Qimantag, East Kunlun Mountains. Chang'an University, Xi'an, pp. 103–130 (in Chinese with English abstract).
- Gao, Y.B., Li, W.Y., Qian, B., Li, K., Li, D.S., He, S.Y., Zhang, Z.W., Zhang, J.W., 2014. Geochronology, geochemistry and Hf isotopic compositions of the granitic rocks related with iron mineralization in Yemaquan deposit, East Kunlun, NW China. *Acta Petrologica Sinica* 30, 1647–1665 (in Chinese with English abstract).
- Gao, Y.B., Li, K., Qian, B., Li, W.Y., Li, D.S., Su, S.S., Zhang, C.G., Zhang, D.M., Wang, S.M., 2015. The genesis of granodiorites and dark enclaves from the Kaerqueka deposit in east Kunlun belt: evidence from zircon U-Pb dating, geochemistry and Sr-Nd-Hf isotopic compositions. *Geol. China* 42, 646–662 (in Chinese with English abstract).
- Goodge, J.W., Vervoort, J.D., 2006. Origin of Mesoproterozoic A-type granites in Laurentia: Hf isotope evidence. *Earth Planet. Sci. Lett.* 243, 711–731.
- Griffin, W.L., Wang, X., Jackson, S.E., Pearson, N.J., O'Reilly, S.Y., 2002. Zircon geochemistry and magma mixing, SE China: in situ analysis of Hf isotopes, Tonglu and Pingtan igneous complexes. *Lithos* 61, 237–269.
- Guo, Z.F., Deng, J.F., Xu, Z.Q., Mo, X.X., Luo, Z.H., 1998. Late Palaeozoic-Mesozoic intracontinental orogenic process and intermediate-acidic igneous rocks from the eastern Kunlun Mountains of northwestern China. *Geoscience* 12, 344–352 (in Chinese with English abstract).
- Hoskin, P.W.O., Black, L.P., 2000. Metamorphic zircon formation by solid-state recrystallization of protolith igneous zircon. *J. Metamorph. Geol.* 18, 423–439.
- Hou, K.J., Li, Y.H., Zou, T.R., Qu, X.M., Shi, Y.R., Xie, G.Q., 2007. Laser ablation-MC-ICP-MS technique for Hf isotope microanalysis of zircon and its geological applications. *Acta Petrologica Sinica* 23, 2595–2604 (in Chinese with English abstract).
- Hou, K.J., Yuan, S.D., 2010. Zircon U-Pb age and Hf isotopic composition of the volcanic and sub-volcanic rocks in the Ningwu basin and their geological applications. *Acta Petrologica Sinica* 26, 888–902 (in Chinese with English abstract).
- Hu, Y., Niu, Y.L., Li, J.Y., Ye, L., Kong, J.J., Chen, S., Zhang, Y., Zhang, G.R., 2015. Petrogenesis and tectonic significance of the late Triassic mafic dikes and felsic volcanic rocks in the East Kunlun Orogenic Belt, Northern Tibet Plateau. *Lithos* 245, 205–222.
- Huang, H., Niu, Y.L., Nowell, G., Zhao, Z.D., Yu, X.H., Zhu, D.C., Mo, X.X., Ding, S., 2014. Geochemical constraints on the petrogenesis of granitoids in the East Kunlun Orogenic belt, northern Tibetan Plateau: implications for continental crust growth through syn-collisional felsic magmatism. *Chem. Geol.* 370, 1–18.
- Irvine, T., Baragar, W., 1971. A guide to the chemical classification of the common volcanic rocks. *Can. J. Earth Sci.* 8, 523–548.
- Jackson, S.E., Pearson, N.J., Griffin, W.L., Belousova, E.A., 2004. The application of laser ablation-inductively coupled plasma-mass spectrometer (LA-ICP-MS) to in situ U-Pb zircon geochronology. *Chem. Geol.* 211, 47–69.
- Jiang, C.F., Yang, J.S., Feng, B.G., Zhu, Z.Z., Zhao, M., Chai, Y.C., Shi, X.D., Wang, H.D., Hu, J.Q., 1992. Opening-closing Tectonics of Kunlun Mountains. Geological Publishing House, Beijing pp. 1–181 (in Chinese with English abstract).
- Kemp, A.I.S., Hawkesworth, C.J., Foster, G.L., Paterson, B.A., Hergt, J.M., Gray, C.M., Whitehouse, M.J., 2007. Magmatic and crustal differentiation history of granitic rocks from Hf-O isotopes in zircon. *Science* 315, 980–983.
- Kuçu, I., Gencalioglu-Kuscu, G., Meinert, L.D., Floyd, P.A., 2002. Tectonic setting and petrogenesis of the Celebi granitoid, (Kirkkale-Turkey) and comparison with world skarn granitoids. *J. Geochem. Explor.* 76, 175–194.
- Kuçu, I., Gencalioglu-Kuscu, G., Sarac, C., Meinert, L.D., 2004. An approach to geochemical characterization of productive versus barren granitoids in terms of iron in Central Turkey. *J. Asian Earth Sci.* 24, 311–325.
- Kwak, T.A.P., White, A.J.R., 1982. Contrasting W-Mo-Cu and W-Sn-F skarn types and related granitoids. *Min. Geol.* 32, 339–351.
- Le Maitre, R.W. (Ed.), 1989. A Classification of Igneous Rocks and Glossary of Terms. Blackwell, Oxford pp. 193.
- Lee, C.T.A., Leeman, W.P., Canil, D., Li, Z.X.A., 2005. Similar V/Sc systematics in MORB and arc basalts: implications for the oxygen fugacities of their mantle source regions. *J. Petrol.* 46 (11), 2313–2336.
- Li, X.H., Long, W.G., Li, Q.L., Liu, Y., Zheng, Y.F., Yang, Y.H., Chamberlain, K.R., Wan, D.F., Guo, C.H., Wang, X.C., Tao, H., 2010. Penglai zircon megacrysts: a potential new working reference material for microbeam determination of Hf-O isotopes and U-Pb age. *Geostand. Geoanal. Res.* 34, 117–134.
- Li, J.X., Qin, K.Z., Li, G.M., Xiao, B., Chen, L., Zhao, J.X., 2011. Post-collisional ore-bearing adakitic porphyries from Gangdese porphyry copper belt, southern Tibet: melting of thickened juvenile lower crust. *Lithos* 126, 265–277.
- Li, X.W., Huang, X.F., Luo, M.F., Dong, G.C., Mo, X.X., 2015. Petrogenesis and geodynamic implications of the Mid-Triassic lavas from East Kunlun, northern Tibetan Plateau. *J. Asian Earth Sci.* 105, 32–47.
- Li, Y.C., Li, B., Chen, J., Zhang, Q.M., 2013. Sr-Nd-Pb isotopic characteristics of ore-bearing granodiorites from Lalingzaohuo deposit and its geological significance. *Mineral. Petrol.* 33, 110–115 (in Chinese with English abstract).
- Liu, C.D., Mo, X.X., Luo, Z.H., Yu, X.H., Chen, H.W., Li, S.W., Zhao, X., 2003. Pb-Sr-Nd-O isotope characteristics of granitoids in East Kunlun orogenic belt. *Acta Geoscientica Sinica* 24, 584–588 (in Chinese with English abstract).
- Liu, H.T., 2001. Qimantag terrestrial volcanics: petrologic evidence of active continental margin of Tarim Plate during late Indo-China epoch. *Acta Petrologica Sinica* 17, 337–351 (in Chinese with English abstract).
- Liu, Y.S., Hu, Z.C., Gao, S., Günther, D., Xu, J., Gao, C.G., Chen, H.H., 2008. In situ analysis of major and trace elements of anhydrous minerals by LA-ICP-MS without applying an internal standard. *Chem. Geol.* 257, 34–43.
- Liu, Y.S., Hu, Z.C., Zong, K.Q., Gao, C.G., Gao, S., Xu, J., Chen, H.H., 2010. Reappraisal and refinement of zircon U-Pb isotope and trace element analyses by LA-ICP-MS. *Chin. Sci. Bull.* 55 (15), 1535–1546.
- Ludwig, K.R., 2003. User's manual for Isoplot 3.0: a geochronological toolkit for Microsoft Excel. Berkeley Geochronology Center Special Publication, 4.
- Ma, C.Q., Xiong, F.H., Yin, S., Wang, L.X., Gao, K., 2015. Intensity and cyclicity of orogenic magmatism: an example from a Paleo-Tethyan granitoid batholith, Eastern Kunlun, northern Qinghai-Tibetan Plateau. *Acta Petrologica Sinica* 31, 3555–3568 (in Chinese with English abstract).
- Mao, J.W., Zhang, Z.C., Zhang, Z.H., Du, A.D., 1999. Re-Os isotopic dating of molybdenites in the Xiaoliugou W (Mo) deposit in the northern Qilian mountains and its geological significance. *Geochim. Cosmochim. Acta* 63, 1815–1818.
- Mao, J.W., Zhou, Z.H., Feng, C.Y., Wang, Y.T., Zhang, C.Q., Peng, H.J., Yu, M., 2012. A preliminary study of the Triassic large-scale mineralization in China and its geodynamic setting. *Geol. China* 39, 1437–1471 (in Chinese with English abstract).
- McDonough, W.F., Sun, S.S., 1995. The composition of the Earth. *Chem. Geol.* 120, 223–253.
- McInnes, B.I.A., Cameron, E.M., 1994. Carbonated, alkaline hybridizing melts from a subarc environment—mantle wedge samples from the Tabar-Lihir Tanga-Feni Arc, Papua-New-Guinea. *Earth Planet. Sci. Lett.* 122 (1–2), 125–141.
- Meinert, L.D., 1992. Skarns and skarn deposits. *Geosci. Can.* 19, 145–162.
- Meinert, L.D., 1993. Igneous petrogenesis and skarn deposits. *Geol. Assoc. Can. Spec. Pap.* 40, 569–583.
- Meinert, L.D., 1995. Compositional variation of igneous rocks associated with skarn deposits—chemical evidence for a genetic connection between petrogenesis and mineralization. In: Thompson, J.F.H. (Ed.), *Magmas, Fluids and Ore Deposits*, vol. 23. Mineralogical Association of Canada Short Course, pp. 401–418.
- Meinert, L.D., Hedenquist, W.J., Satoh, H., Matsuhisa, Y., 2003. Formation of anhydrous and hydrous skarn in Cu-Au ore deposit by magmatic fluids. *Econ. Geol.* 98, 147–156.
- Meinert, L.D., Dipple, G.M., Nicolescu, S., 2005. World skarn deposits. *Economic Geology* 100th Anniversary Volume, 299–366.
- Meng, X.Y., Mao, J.W., Zhang, C.Q., Zhang, D.Y., Kong, Z.G., Jia, F.D., 2016. The timing, origin and T-f₀₂ crystallization conditions of long-lived magmatism at the Yangla copper deposit, Sanjiang Tethyan orogenic belt: Implications for post-collisional magmatic-hydrothermal ore formation. *Gondwana Res.* 40, 211–229.
- Mo, X.X., Luo, Z.H., Deng, J.F., Yu, X.H., Liu, C.D., Chen, H.W., Yuan, W.M., Liu, Y.H., 2007. Granitoids and crustal growth in the East-Kunlun orogenic belt. *Geol. J. China Universities* 13, 403–414 (in Chinese with English abstract).
- Morel, M.L.A., Nebel, O., Nebel-Jacobsen, Y.J., Miller, J.S., Vroon, P.Z., 2008. Hafnium isotope characterization of the GJ-1 zircon reference material by solution and laser-ablation MC-ICPMS. *Chem. Geol.* 255, 231–235.
- Mungall, J.E., 2002. Roasting the mantle: slab melting and the genesis of major Au and Au-rich Cu deposits. *Geology* 30 (10), 915–918.
- Murgulov, V., O'Reilly, S.Y., Griffin, W.L., Blevin, P.L., 2008. Magma sources and gold mineralization in the Mount Leyshon and Tuckers Igneous Complexes, Queensland Australia: U-Pb and Hf isotope evidence. *Lithos* 101, 281–307.
- Nakano, T., Shimazaki, H., Shimizu, M., 1990. Strontium isotope systematics and metallogenesis of skarn deposits in Japan. *Econ. Geol.* 85, 794–815.
- Pang, K.N., Zhou, M.F., Lindsley, D., Zhao, D.G., Malpas, J., 2008. Origin of Fe-Ti oxide ores in mafic intrusions: evidence from the Panzhihua intrusion, SW China. *J. Petrol.* 49, 295–313.
- Pearce, J.A., Harris, N.B.W., Tindle, A.G., 1984. Trace element discrimination diagrams for the tectonic interpretation of granitic rocks. *J. Petrol.* 25, 956–983.
- Pettke, T., Audétat, A., Schaltegger, U., Heinrich, C.A., 2005. Magmatic-to-hydrothermal crystallization in the W-Sn mineralized Mole Granite (NSW, Australia): part II: evolving zircon and thorite trace element chemistry. *Chem. Geol.* 220, 191–213.
- Pons, J., Franchini, M., Meinert, L., López-Escobar, L., Maydagán, L., 2010. Geology, petrography and geochemistry of igneous rocks related to mineralized skarns in the NW Neuquén basin, Argentina: implications for Cordilleran skarn exploration. *Ore Geol. Rev.* 38, 37–58.
- Qiu, K.F., Deng, J., 2016. Petrogenesis of granitoids in the Dewulu skarn copper deposit: implications for the evolution of the Paleotethys ocean and mineralization in Western Qinqing, China. *Ore Geol. Rev.* <http://dx.doi.org/10.1016/j.oregeorev.2016.09.027>.
- Qiu, K.F., Taylor, R.D., Song, Y.H., Yu, H.C., Song, K.R., Li, N., 2016. Geologic and geochemical insights into the formation of the Taiyangshan porphyry copper-molybdenum deposit, Western Qinqing Orogenic Belt, China. *Gondwana Res.* 35, 40–58.
- Ray, G.E., Webster, I.C.L., Ettlinger, A.D., 1995. The distribution of skarns in British Columbia and the chemistry and ages of their related plutonic rocks. *Econ. Geol.* 90, 920–937.
- Reynolds, I.M., 1985. The nature and origin of titaniferous magnetite-rich layers in the upper zone of the Bushveld complex: a review and synthesis. *Econ. Geol.* 80 (4), 1089–1108.
- Richards, J.P., 2015. The oxidation state, and sulfur and Cu contents of arc magmas: implications for metallogenesis. *Lithos* 233, 27–45.
- Shaw, S.E., Flood, R.H., 2009. Zircon Hf isotopic evidence for mixing of crustal and silicic mantle-derived magmatism a zoned granite pluton, Eastern Australia. *J. Petrol.* 50, 147–168.
- Shimazaki, H., Yamamoto, M., 1983. Sulfur isotope ratios of the Akatani, Iide and Wagassen skarn deposits, and their bearing on mineralizations in the “Green Tuff” region, Japan. *Geochim. J.* 17, 197–207.
- Sillitoe, R.H., 2010. Porphyry copper systems. *Econ. Geol.* 105 (1), 3–41.
- Sláma, J., Košler, J., Condon, D.J., Crowley, J.L., Gerdes, A., Hanchar, J.M., Horstwood, M.S.A., Morris, G.A., Nasdala, L., Norberg, N., Schaltegger, U., Schoene, B., Tubrett, M.N., Whitehouse, M.J., 2008. Plesovice zircon—a new natural reference material for U-Pb and Hf isotopic microanalysis. *Chem. Geol.* 249, 1–35.

- Stein, H.J., Markey, R.J., Morgan, J.W., Hannah, J.L., Scherstén, A., 2001. The remarkable Re-Os chronometer in molybdenite: how and why it works. *Terra Nova* 13, 479–486.
- Sun, W.D., Huang, R.F., Li, H., Hu, Y.B., Zhang, C.C., Sun, S.J., Zhang, L.P., Ding, X., Li, C.Y., Zartman, R.E., Ling, M.X., 2015. Porphyry deposits and oxidized magmas. *Ore Geol. Rev.* 65, 97–131.
- Tian, C.S., Feng, C.Y., Li, J.H., Cao, D.Z., 2013. ^{40}Ar - ^{39}Ar geochronology of Tawenchahan Fe-polymetallic deposit in Qimantag Mountain of Qinghai Province and its geological implications. *Miner. Deposits* 32 (1), 169–176 (in Chinese with English abstract).
- Trail, D., Watson, E.B., Tailby, N.D., 2012. Ce and Eu anomalies in zircon as proxies for the oxidation state of magmas. *Geochim. Cosmochim. Acta* 97, 70–87.
- Wang, S., Feng, C.Y., Li, S.J., Jiang, J.H., Li, D.S., Su, S.S., 2009. Zircon SHRIMP U-Pb dating of granodiorite in the Kaerqueka polymetallic ore deposit, Qimantag Mountain, Qinghai Province, and its geological implications. *Geol. China* 36, 74–84 (in Chinese with English abstract).
- Wang, F.C., Chen, J., Xie, Z., Li, S.P., Tan, S.X., Zhang, Y.B., Wang, T., 2013. Geological features and Re-Os isotopic dating of the Lalingzaohuo molybdenum polymetallic deposit in East Kunlun. *Geol. China* 40, 1209–1217 (in Chinese with English abstract).
- Wang, G., Sun, F.Y., Li, B.L., Li, S.J., Zhao, J.W., Yang, Q.A., 2014. Zircon U-Pb geochronology and geochemistry of diorite in Xiarihamu ore district from East Kunlun and its geological significance. *J. Jilin University (Earth Science Edition)* 44, 876–891 (in Chinese with English abstract).
- Wong, J., Sun, M., Xing, G.F., Li, X.H., Zhao, G.C., Wong, K., Yuan, C., Xia, X.P., Li, L.M., Wu, F.Y., 2009. Geochemical and zircon U-Pb and Hf isotopic study of the Baijuhuajian metaluminous A-type granite, Extension at 125–100 Ma and its tectonic significance for South China. *Lithos* 112, 289–305.
- Wu, F.Y., Yang, Y.H., Xie, L.W., Yang, J.H., Ping, X., 2006. Hf isotopic compositions of the standard zircons and baddeleyites used in U-Pb geochronology. *Chem. Geol.* 234, 105–126.
- Wu, F.Y., Li, X.H., Zheng, Y.F., Gao, S., 2007. Lu-Hf isotopic systematics and their applications in petrology. *Acta Petrologica Sinica* 23, 185–220 (in Chinese with English abstract).
- Wu, X.K., Meng, F.C., Xu, H., Cui, M.H., 2011. Zircon U-Pb dating, geochemistry and Nd-Hf isotopic compositions of the Maxingdaban Late Triassic granitic pluton from Qimantag in the eastern Kunlun. *Acta Petrologica Sinica* 27, 3380–3394 (in Chinese with English abstract).
- Xi, R.G., Xiao, P.X., Wu, Y.Z., Dong, Z.C., Guo, L., Gao, X.F., 2010. The Geological significances, composition and age of the monzonitic granite in Kendekeke iron mine. *Northwestern Geol.* 43, 195–202 (in Chinese with English abstract).
- Xia, R., Wang, C.M., Qing, M., Deng, J.M., Carranza, E.J., Li, W.L., Guo, X.D., Ge, L.S., Yu, W.Q., 2015a. Molybdenite Re-Os, zircon U-Pb dating and Hf isotopic analysis of the Shuangqing Fe-Pb-Zn-Cu skarn deposit, East Kunlun Mountains, Qinghai Province, China. *Ore Geol. Rev.* 66, 114–131.
- Xia, R., Wang, C.M., Qing, M., Li, W.L.M., Carranza, E.J., Guo, X.D., Ge, L.S., Zeng, G.Z., 2015b. Zircon U-Pb dating, geochemistry and Sr-Nd-Pb-Hf-O isotopes for the Nangetan granodiorites and mafic microgranular enclaves in the East Kunlun Orogen: Record of closure of the Paleo-Tethys. *Lithos* 234–235, 47–60.
- Xiao, Y., Feng, C.Y., Liu, J.N., Yu, M., Zhou, J.H., Li, D.X., Zhao, Y.M., 2013. LA-MC-ICP-MS zircon U-Pb dating and sulfur isotope characteristics of Kendekeke Fe-polymetallic deposit, Qinghai Province. *Miner. Deposits* 32, 177–186 (in Chinese with English abstract).
- Xie, G.Q., Mao, J.W., Zhao, H.J., 2011. Zircon U-Pb geochronological and Hf isotopic constraints on petrogenesis of Late Mesozoic intrusions in the southeast Hubei Province, Middle-Lower Yangtze River belt (MLYRB), East China. *Lithos* 125, 693–710.
- Xie, G.Q., Mao, J.W., Zhu, Q.Q., Yao, L., Li, Y.H., Li, W., Zhao, H.J., 2015. Geochemical constraints on Cu-Fe and Fe skarn deposits in the Edong district, Middle-Lower Yangtze River metallogenetic belt, China. *Ore Geol. Rev.* 64, 425–444.
- Xie, G.Q., Mao, J.W., Li, W., Zhu, Q.Q., Liu, H.B., Jia, G.H., Li, Y.H., Li, J.J., Zhang, J., 2016. Different proportion of mantle-derived noble gases in the Cu-Fe and Fe skarn deposits: He-Ar isotopic constraint in the Edong district, Eastern China. *Ore Geol. Rev.* 72, 343–354.
- Xiong, F.H., Ma, C.Q., Zhang, J.Y., Liu, B., Jiang, H.A., Huang, J., 2011. Zircon LA-ICP-MS U-Pb dating of Bairiqili gabbro pluton in East Kunlun orogenic belt and its geological significance. *Geol. Bull. China* 30, 1196–1202 (in Chinese with English abstract).
- Xu, Z.Q., Yang, J.S., Li, H.B., Zhang, J.X., Wu, C.L., 2007. Orogenic plateau-terrace amalgamation, collision and uplift in the Qinghai-Tibet plateau. Geological Publishing House, Beijing, pp. 1–7 (in Chinese with English abstract).
- Xu, Q.L., Sun, F.Y., Li, B.L., Qian, Ye., Li, L., Yang, Y.Q., 2014. Geochronological Dating, Geochemical Characteristics and Tectonic Setting of the Granite-porphyry in the Mohejiala Silver Polymetallic Deposit, Eastern Kunlun Orogenic Belt. *Geotectonica et Metallogenesis* 38, 421–433.
- Yang, J.H., Wu, F.Y., Wilde, S.A., Xie, L.W., Yang, Y.H., Liu, X.M., 2007. Tracing magma mixing in granite genesis: in situ U-Pb dating and Hf-isotope analysis of zircons. *Contrib. Miner. Petrol.* 153, 177–190.
- Yang, X.L., Lee, I., 2011. Review of the stable isotope geochemistry of Mesozoic igneous rocks and Cu-Au deposits along the middle-lower Yangtze metallogenetic belt, China. *International Geology Review* 53, 741–757.
- Yang, T., 2015. Geological characteristics and genesis discussion of the Tawenchahanxi Fe-polymetallic deposit in Qimantag area, Qinghai province. Chang'an University, Chang'an, pp. 32–42 (in Chinese with English abstract).
- Yao, L., 2015. Petrogenesis of the Triassic granitoids and skarn mineralization in the Qimantag area, Qinghai Province, and their geodynamic setting. China University of Geosciences, Beijing, pp. 88–91 (in Chinese with English abstract).
- Yao, L., Xie, G.Q., Mao, J.W., Lü, Z.C., Zhao, C.S., Zheng, X.W., Ding, N., 2015a. Geological, geochronological, and mineralogical constraints on the genesis of the Chengchao skarn Fe deposit, Edong ore district, Middle-Lower Yangtze River Valley metallogenetic belt, eastern China. *J. Asian Earth Sci.* 101, 68–82.
- Yao, L., Lü, Z.C., Yu, X.F., Pang, Z.S., Li, Y.S., Jiang, W., Li, D.S., Liu, P., 2015b. Mineral characteristics of granitic rocks from skarn deposits, Qimantag area, Qinghai Province, East Kunlun, and its geological significance. *Acta Petrologica Sinica* 31, 2294–2306.
- Yao, L., Lü, Z.C., Yu, X.F., Pang, Z.S., Cai, Y.Q., Liu, P., Liu, C.C., Wang, F.L., 2015c. Petrogenesis, geochemistry and zircon U-Pb age of the granite from No. VI section of Hutouya deposit, Qimantag area, Qinghai Province, and its geological significance. *J. Jilin University (Earth Science Edition)* 45, 743–758.
- Yu, M., 2013. Geochemistry and Zonation of the Galinge Iron Deposit, Qinghai Province. China University of Geosciences, Beijing, pp. 68–69 (in Chinese with English abstract).
- Yu, M., Feng, C.Y., Liu, H.C., Li, D.W., Zhao, Y.M., Li, D.X., Liu, J.N., Wang, H., Zhang, M.H., 2015a. ^{40}Ar - ^{39}Ar geochronology of the Galinge large skarn iron deposit in Qinghai Province and geological significance. *Acta Geol. Sinica* 89, 510–521 (in Chinese with English abstract).
- Yu, M., Feng, C.Y., Zhao, Y.M., Li, D.X., 2015b. Genesis of post-collisional calc-alkaline and alkaline granitoids in Qiman Tagh, East Kunlun, China. *Lithos* 239, 45–59.
- Yu, M., Feng, C.Y., Santosh, M., Mao, J.W., Zhu, Y.F., Zhao, Y.M., Li, D.X., Li, B., 2017. The Qiman Tagh Orogen as a window to the crustal evolution in northern Qinghai-Tibet Plateau. *Earth Sci. Rev.* 167, 103–123.
- Yu, N., Jin, W., Ge, W.C., Long, X.P., 2005. Geochemical study on peraluminous granite from Jinshukou in East Kunlun. *Global Geol.* 24, 123–128 (in Chinese with English abstract).
- Zhang, A.K., Liu, G.L., Feng, C.Y., Mo, X.X., Yang, L.C., Liu, Y.L., He, S.Y., Ma, Y.S., 2013. Geochemical characteristics and ore-controlling factors of Hutouya polymetallic deposit, Qinghai Province. *Miner. Deposits* 32 (1), 94–108 (in Chinese with English abstract).
- Zhang, C.C., Sun, W.D., Wang, J.T., Zhang, L.P., Sun, S.J., Wu, K., 2017. Oxygen fugacity and porphyry mineralization: a zircon perspective of Dexing porphyry Cu deposit, China. *Geochim. Cosmochim. Acta* 206, 343–363.
- Zhao, Y.M., Lin, W.W., Bi, C.S., Li, D.X., Jiang, C.J., 2012. Skarn deposits of China. Geological Publishing House, Beijing, pp. 1–392 (in Chinese with English abstract).
- Zhao, Y.M., Feng, C.Y., Li, D.X., Liu, J.N., Xiao, Y., Yu, M., Ma, S.C., 2013. Metallogenetic setting and mineralization-alteration characteristics of major skarn Fe-polymetallic deposits in Qimantag area, western Qinghai Province. *Mineral Deposits* 32, 1–19 (in Chinese with English abstract).
- Zharikov, V.A., 1970. Skarns. *Int. Geol. Rev.* 12, 541–559, 619–647, and 760–775.
- Zhou, T.F., Yuan, F., Yue, S.C., Liu, X.D., Zhang, X., Fan, Y., 2007. Geochemistry and evolution of ore-forming fluids of the Yueshan Cu-Au skarn- and vein-type deposits, Anhui Province, South China. *Ore Geol. Rev.* 31, 279–303.
- Zuo, P.F., Liu, X.F., Hao, J.H., Wang, Y.S., Zhao, R., Ge, S.S., 2015. Chemical compositions of garnet and clinopyroxene and their genetic significances in Yemaquan skarn iron-copper-zinc deposit, Qimantag, eastern Kunlun. *J. Geochem. Explor.* 158, 143.